Submitted to

31st International Conference on High Energy Physics, ICHEP02, July 24, 2002, Amsterdam
Abstract: **980**
Parallel Session **6**

www-h1.desy.de/h1/www/publications/conf/conf_list.html

Measurement and NLO DGLAP QCD Interpretation of Diffractive Deep-Inelastic Scattering at HERA

H1 Collaboration

Abstract

A high precision inclusive measurement of the diffractive deep inelastic scattering (DIS) process $ep \to eXY$ is presented, where Y is a proton or a low mass proton excitation carrying a fraction $1 - x_{I\!P} > 0.95$ of the beam longitudinal momentum and the squared 4-momentum transfer at the proton vertex $t > -1\ \mathrm{GeV}^2$. The measurement, based on an integrated luminosity of $10.6\ \mathrm{pb}^{-1}$, is presented in the form of a diffractive reduced cross section $\sigma_r^{D(3)}$, measured in the kinematic range $6.5 \leq Q^2 \leq 120\ \mathrm{GeV}^2$, $0.01 \leq \beta \leq 0.9$ and $10^{-4} \lesssim x_{I\!P} < 0.05$. The ratio of the diffractive to the inclusive cross section $\sigma_r^{D(3)}(x, Q^2, x_{I\!P})/\sigma_r(x, Q^2)$ is measured and found to be remarkably flat as a function of Q^2 with x and $x_{I\!P}$ fixed. The measured cross section is compared with various models for diffractive DIS. The $x_{I\!P}$ dependence of the data is interpreted in terms of a measurement of the effective pomeron intercept $\alpha_{I\!P}(0) = 1.173\ \pm 0.018\ (\mathrm{stat.})\ \pm 0.017\ (\mathrm{syst.})\ ^{+0.063}_{-0.035}\ (\mathrm{model})$. A NLO DGLAP QCD fit is performed to the data, together with an assessment of the experimental and theoretical uncertainties on the resulting diffractive parton densities. The diffractive exchange is shown to be dominated by the diffractive gluon density, which carries an integrated fraction $75 \pm 15\%$ of the exchanged momentum at $Q^2 = 10\ \mathrm{GeV}^2$ and extends to large fractional momenta. The parton densities are used to make updated comparisons with diffractive dijet and open charm cross sections at HERA and the Tevatron, thus testing the factorisation properties of hard diffraction.

1 Introduction

Although Quantum Chromodynamics (QCD) is the well established gauge theory of strong interactions, perturbative QCD calculations are only possible for short distance, hard partonic interactions, where the strong coupling α_s is small. On the other hand, hadronic cross sections at high centre-of-mass energies are dominated by soft interactions, for which perturbation theory is inapplicable. A large fraction of these soft interactions are mediated by colour-singlet exchange and are termed *diffractive*. The observation of hard sub-processes in diffractive events [1] introduces the exciting possibility of understanding the diffractive exchange in terms of parton dynamics, which would represent an important step towards a deeper understanding of soft strong interactions and of confinement.

Diffractive processes of the type $ep \to eXp$ have been extensively studied in deep-inelastic electron-proton scattering (DIS) at low x at the HERA collider [2–7]. In these events, the structure of colour-singlet exchange is probed using point-like highly virtual photons. A hard scattering QCD factorisation theorem was recently proven for a general class of semi-inclusive DIS processes, which include the process $ep \to eXp$ [8]. This implies that the concept of 'diffractive parton distributions' [9] can be introduced, expressing conditional proton parton probability distributions under the constraint of a leading baryonic system of particular 4-momentum. This allows diffractive DIS to be tackled with a similar theoretical description to inclusive DIS, namely the framework of the next-to-leading order (NLO) DGLAP [10] evolution equations.

In this paper, a high precision measurement of the diffractive DIS cross section is presented, based upon data collected with the H1 detector at HERA. This new measurement, first reported in [6], yields a significant increase in precision compared with previous H1 [3] and ZEUS [4] data. A NLO DGLAP QCD fit is performed to the data. For the first time an assessment of the experimental and theoretical uncertainties on the resulting diffractive parton densities is made. To test the validity of QCD hard scattering factorisation as applied to diffraction, the parton densities are used for comparisons with diffractive DIS dijet [11] and open charm [12] cross sections at HERA as well as with diffractive dijet production at the Tevatron [13]. The ratio of the diffractive to the total DIS cross section is also investigated and the data are compared with various theoretical models for the diffractive exchange.

1.1 Kinematics of Diffractive DIS at HERA

Figure 1 illustrates the generic diffractive process at HERA of the type $ep \to eXY$. The electron (with 4-momentum k) couples to a virtual photon (q) which interacts with the proton (P). The usual DIS kinematic variables are defined as

$$Q^2 = -q^2 \; ; \qquad y = \frac{P \cdot q}{P \cdot k} \; ; \qquad x = \frac{-q^2}{2P \cdot q} \; , \tag{1}$$

where Q^2 is the photon virtuality, x corresponds to the longitudinal momentum fraction of the struck quark with respect to the proton and y is the inelasticity variable. The squared invariant masses of the electron-proton and photon-proton systems s and W^2 are given by

$$s = (k + P)^2 \simeq (300 \text{ GeV})^2 \; ; \qquad W^2 = (q + P)^2 \simeq ys - Q^2 \; . \tag{2}$$

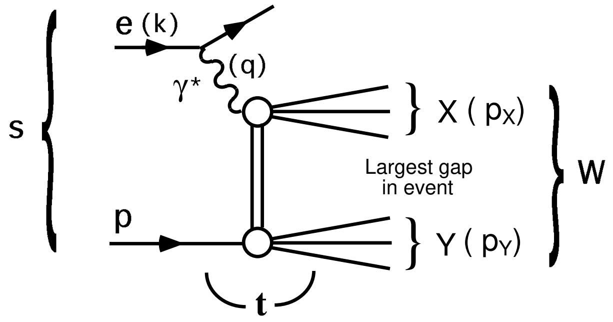

Figure 1: The generic diffractive process at HERA, where the electron (four-momentum k) couples to a photon (q) which interacts with the proton (P) via net colour singlet exchange, producing two distinct final state hadronic systems X and Y.

If the interaction takes place via colour singlet exchange, the photon and proton dissociate to produce distinct hadronic systems X and Y, with invariant masses M_X and M_Y respectively. In the case where M_X and M_Y are small compared with W, the two systems are separated by a large rapidity gap. The longitudinal momentum fraction $x_{I\!P}$ of the colourless exchange with respect to the incoming proton and the squared four-momentum transferred at the proton vertex t are then defined by

$$x_{I\!P} = \frac{q \cdot (P - p_Y)}{q \cdot P} = \frac{Q^2 + M_X^2 - t}{Q^2 + W^2 - M_p^2} \; ; \qquad t = (P - p_Y)^2 \; , \tag{3}$$

where p_Y is the 4-momentum of Y. In addition, the quantity β is defined as

$$\beta = \frac{x}{x_{I\!P}} = \frac{Q^2}{2q \cdot (P - p_Y)} = \frac{Q^2}{Q^2 + M_X^2 - t} \; . \tag{4}$$

In an interpretation in which partonic structure is ascribed to the colourless exchange, β is the longitudinal momentum fraction of the exchange that is carried by the struck quark, in analogy to x in the case of inclusive scattering.

1.2 Diffractive Reduced Cross Section and Structure Functions

The cross section for the diffractive DIS process $ep \to eXY$ depends in general on 5 independent variables (neglecting azimuthal angles). Here, we work with Q^2,x (or β), $x_{I\!P}$, M_Y and t. The system Y is not measured in this analysis and the results are integrated over $|t| < 1.0\ \mathrm{GeV}^2$ and $M_{_Y} < 1.6\ \mathrm{GeV}$. They are expressed in terms of a *reduced diffractive cross section* $\sigma_r^{D(3)}$, defined through

$$\frac{d^3\sigma^D}{\mathrm{d}x_{I\!P}\,\mathrm{d}x\,\mathrm{d}Q^2} = \frac{4\pi\alpha^2}{xQ^4}\left(1 - y + \frac{y^2}{2}\right)\sigma_r^{D(3)}(x_{I\!P}, x, Q^2) \; . \tag{5}$$

Neglecting contributions from Z^0 exchange, $\sigma_r^{D(3)}$ is related to the diffractive structure functions $F_2^{D(3)}$ and $F_L^{D(3)}$ by

$$\sigma_r^{D(3)} = F_2^{D(3)} - \frac{y^2}{1 + (1-y)^2} F_L^{D(3)} \; , \tag{6}$$

where F_L^D is the longitudinal diffractive structure function. The positivity constraint on the cross sections for longitudinally and transversely polarised photon scattering leads to the relation $0 \leq F_L^D \leq F_2^D$. The contribution of F_L^D to $\sigma_r^{D(3)}$ can be sizeable only at large values of y, and in most of the kinematic range the relation $\sigma_r^{D(3)} \approx F_2^D$ holds to good approximation. In previous measurements of inclusive diffractive DIS at HERA [3,4], the data were presented in terms of F_2^D and F_L^D was neglected.

1.3 Factorisation in Diffraction

The proof that QCD hard scattering factorisation can be applied to diffractive DIS [8] implies that in the leading $\log(Q^2)$ approximation, the cross section for the diffractive process $\gamma^* p \to XY$ can be written in terms of convolutions of universal partonic cross sections $\hat{\sigma}^{\gamma^* i}$ with *diffractive parton distributions* f_i^D [9], representing probability distributions for a parton i in the proton under the constraint that the proton is scattered with particular values of t and $x_{I\!P}$. Thus, at leading twist,[1]

$$\frac{\mathrm{d}^2\sigma(x, Q^2, x_{I\!P}, t)^{\gamma^* p \to p' X}}{\mathrm{d}x_{I\!P}\, \mathrm{d}t} = \sum_i \int_x^{x_{I\!P}} \mathrm{d}\xi \, \hat{\sigma}^{\gamma^* i}(x, Q^2, \xi) \, f_i^D(\xi, Q^2, x_{I\!P}, t) \, . \tag{7}$$

The factorisation formula is valid for large enough Q^2 and fixed $x_{I\!P}$ and t. It also applies to the case of proton dissociation into a system of fixed mass M_Y. The partonic cross sections $\hat{\sigma}^{\gamma^* i}$ are the same as those for inclusive DIS and the diffractive parton distributions f_i^D, which are not known from first principles, should obey the DGLAP [10] evolution equations.

In addition to the rigorous theoretical prescription represented by equation (7), an additional assumption is often made, that the shape of the diffractive parton distributions is independent of $x_{I\!P}$ and t and that their normalisation is controlled by Regge asymptotics [15]. The diffractive parton distributions can then be factorised into a term depending only on $x_{I\!P}$ and t and a second term depending only on x (or β) and Q^2:

$$f_i^D(x_{I\!P}, t, x, Q^2) = f_{I\!P/p}(x_{I\!P}, t) \cdot f_i^{I\!P}(\beta = x/x_{I\!P}, Q^2) \, . \tag{8}$$

Under this *Regge* factorisation assumption, often referred to in the literature as the *Ingelman-Schlein* or *resolved pomeron* model, the diffractive exchange can be treated as a quasi-real object with a partonic structure, given by parton distributions $f_i^{I\!P}(\beta, Q^2)$. The variable β then corresponds to the longitudinal momentum fraction of the diffractive exchange carried by the struck parton in the *pomeron*. The *pomeron flux factor* $f_{I\!P/p}(x_{I\!P}, t)$ represents the probability that a pomeron with particular values of $x_{I\!P}$ and t couples to the proton. Although equation (8) has no firm basis in QCD, at the present level of precision it appears to be supported by data [3,4,6].

Various fits to diffractive DIS data have been performed under the assumptions of both QCD hard scattering and Regge factorisation [3, 16–18], using the DGLAP equations to evolve the diffractive parton distributions. In [3], previous H1 data for $F_2^{D(3)}$ were fitted. $80 - 90\%$ of the exchanged momentum was found to be carried by gluons. Two fits, usually referred to as 'H1

[1] A framework also exists to include higher order operators [14].

fit 2' and 'H1 fit 3', with slightly different assumptions for the parameterisation of the gluon density at the starting scale, were presented. The factorisation properties of diffractive DIS have been tested by comparing predictions using these parton distributions with diffractive final state observables, such as jet [11] and heavy quark [12] cross sections.

2 Experimental Technique

The data used for the measurement presented in this paper were taken in 1997 using the H1 detector, when HERA collided protons of energy $E_p = 820\,\mathrm{GeV}$ with positrons[2] of energy $E_e = 27.5\ \mathrm{GeV}$. For $Q^2 > 13.5\ \mathrm{GeV}^2$, a luminosity of $10.6\ \mathrm{pb}^{-1}$ is used in the analysis, yielding an increase in statistics relative to previous measurements [3, 4] by a factor of approximately 5. For the region $6.0 < Q^2 < 13.5\ \mathrm{GeV}^2$, a sample of $2.0\ \mathrm{pb}^{-1}$ is used, taken during a period when the experiment ran with dedicated triggers for low Q^2 DIS.

2.1 The H1 Detector

A full description of the H1 apparatus can be found in [19]. Here, only the parts of the detector relevant for the present analysis are briefly discussed. The coordinate system used is such that $\theta = 0$ corresponds to the direction of the outgoing proton beam. The region of low θ and large pseudorapidity $\eta = -\ln\tan\theta/2$ is referred to as the 'forward' direction.

The interaction region is surrounded by the tracking system. Two large concentric drift chambers (CJC), located within a solenoidal magnetic field of $1.15\ \mathrm{T}$, measure the trajectories of charged particles in the range $-1.5 < \eta < 1.5$. A highly segmented Liquid Argon (LAr) calorimeter, covering the range $-1.5 < \eta < 3.4$, surrounds the tracking chambers. The backward direction ($-4.0 < \eta < -1.4$) is covered by a lead / scintillating fibre calorimeter (SPACAL). Both the LAr and the SPACAL calorimeters contain both electromagnetic and hadronic sections. In front of the SPACAL, the Backward Drift Chamber (BDC) provides track segments for charged particles. The ep luminosity is determined by comparing the measured event rate in a photon tagger calorimeter close to the beam pipe at $z = -103\ \mathrm{m}$ with the QED Bremsstrahlung ($ep \rightarrow ep\gamma$) cross section.

To enhance the sensitivity to hadronic activity in the region of the outgoing proton, the PLUG calorimeter, the Forward Muon Detector (FMD) and the Proton Remnant Tagger (PRT) are used. The copper-silicon calorimeter PLUG enables energy measurements to be made in the pseudorapidity range $3.5 < \eta < 5.5$. The FMD is located at $z = 6.5\ \mathrm{m}$ and covers the range $1.9 < \eta < 3.7$ directly. Particles produced at larger η can also be detected because of secondary scattering with the beam-pipe. The PRT, a set of scintillators surrounding the beam pipe at $z = 26\ \mathrm{m}$, tags charged particles in the region $6.0 \lesssim \eta \lesssim 7.5$.

[2]From now on, the word 'electron' will be used as a generic term for electrons and positrons.

2.2 Event Selection and Kinematic Reconstruction

The data were triggered principally on the basis of an energetic cluster in the electromagnetic section of the SPACAL calorimeter, for which the efficiency is close to 100% throughout the measured kinematic region. Events are accepted for the analysis if they contain a scattered electron candidate with energy $E'_e > 6.5$ GeV and polar angle in the range $156^\circ < \theta_e < 176.5^\circ$. To suppress background from photons and hadrons, cuts on the lateral extension of the cluster forming the electron candidate and its containment within the electromagnetic part of the SPACAL are applied. A reconstructed charged track in the BDC, linked within a transverse distance of 3 cm to the SPACAL cluster is requested. A reconstructed event vertex within 30 cm of the nominal interaction point is required from the Central Tracking Detector. The hadronic final state is measured from the hadronic activity in the SPACAL and Liquid Argon calorimeters and the tracking detectors using a method that combines tracks and calorimeter deposits without double counting [20]. A minimum of two reconstructed hadronic final state particles are required for the analysis.

The reconstruction of kinematic variables is performed using very similar techniques to those described in [3]. To reconstruct y, Q^2 and x, a mixed method is used: y is reconstructed as

$$y = y_e^2 + y_d\,(1 - y_d)\,, \tag{9}$$

where y_e and y_d are obtained from the scattered electron only ('electron method') or from the angles of the electron and the hadronic final state ('double angle method'), respectively. The reconstruction method limits to the electron method at high y and the double angle method at low y. Q^2 and x are then computed from

$$Q^2 = \frac{4E_e^2\,(1-y)}{\tan^2(\theta_e/2)}\,; \qquad x = \frac{Q^2}{s\,y}\,. \tag{10}$$

Events where $Q^2 > 5.7$ GeV^2 and $y > 0.04$ enter the final inclusive DIS sample.

Diffractive events are selected on the basis of a large rapidity gap separating the leading baryonic system Y from the photon dissociation system X. The rapidity gap is identified by the absence of activity in detectors sensitive to forward energy flow. The region of the main Liquid Argon Calorimeter with $\eta > 3.2$ must show no energy deposits above noise levels. There must also be no activity above noise thresholds in the PRT, FMD and PLUG detectors. This selection ensures that the X system is well contained in the central part of the detector and is separated by a large rapidity gap covering at least $3.2 < \eta < 7.5$ from the Y system.

The mass of the system X is obtained from the hadronic final state using

$$M_x^2 = 1.08 \cdot (E^2 - p_x^2 - p_y^2 - p_z^2)_{\rm had} \cdot \frac{y}{y_h}\,, \tag{11}$$

where the subscript 'had' represents a sum over all reconstructed hadrons and $y_h = (E - p_z)_{\rm had}/2E_e$. This method of $M_{\rm X}$ reconstruction reduces essentially to a measurement of the total $E + p_z$ of the hadronic final state in the limit of high y, where losses in the backward direction become significant. The global factor of 1.08 accounts for residual losses. The diffractive variables β and $x_{I\!P}$ are then reconstructed using

$$\beta = \frac{Q^2}{Q^2 + M_{\rm X}^2 - t}\,; \qquad x_{I\!P} = \frac{x}{\beta}\,. \tag{12}$$

2.3 Monte Carlo Simulation and Backgrounds

Corrections for detector inefficiencies, acceptances and migrations between measurement intervals are performed using a Monte Carlo simulation which combines several different models. The RAPGAP 2.08 [21] model is used to simulate colour-singlet exchange processes with $x_{I\!P} < 0.15$, based on the 'resolved pomeron model' QCD fits in [3], including contributions from pomeron and sub-leading meson exchange. Specifically, the 'fit 2' parton distributions for the pomeron are used, evolved using Q^2 as a scale and convoluted with leading order QCD matrix elements. Parton showers [22] in the leading $\log(Q^2)$ approximation are used to approximate higher order QCD effects. Hadronisation is simulated using the Lund string model in JETSET [23]. QED radiative effects are taken into account via an interface to the HERACLES program [24].

The DIFFVM model [25] is used to simulate the quasi elastic production of the ρ, ω, ϕ and J/ψ vector mesons, which contribute at small M_X (high β). Smearing from the region $x_{I\!P} > 0.15$ is modelled using the DJANGO [26] Monte Carlo model for standard DIS, based on recent structure function data [27]. The small QED-Compton background at the largest β is subtracted using the COMPTON [28] Monte Carlo model. Photoproduction background, which is negligible except at the highest y values, is subtracted using the PHOJET [29] model.

2.4 Cross Section Measurement and Structure Function Extraction

The large rapidity gap selection yields a sample dominated by the single dissociation process $ep \rightarrow eXp$, with a small admixture of double dissociation events of the type $ep \rightarrow eXY$ where the proton dissociation system has a small mass $M_{\rm Y}$. The measurement is corrected to the region $M_{\rm Y} < 1.6$ GeV and $|t| < 1$ GeV^2, as was the case for previous H1 data [3]. The correction factor applied to account for smearing about the $M_{\rm Y}$ and t boundaries of the measurement is $-8.7 \pm 8.2\%$, as evaluated using the DIFFVM model of elastic and proton dissociative processes. The final cross sections correspond to the case where the systems X and Y are separated by the largest gap in the rapidity distribution of the final state hadrons. The triple differential reduced cross section $\sigma_r^{D(3)}(x, Q^2, x_{I\!P})$ is extracted according to equation 5. Corrections for initial and final state electromagnetic radiation and QED virtual loops are performed using the RAPGAP Monte Carlo model via an interface to HERACLES [24]. The final measurements are quoted at the Born level.

The measurement is performed using various binning schemes which are optimised to the study of different aspects of the data. To investigate the $x_{I\!P}$ dependence for example, the cross section is measured in many $x_{I\!P}$ intervals. By contrast, the x, β and Q^2 dependences of $\sigma_r^{D(3)}$ and their variation with $x_{I\!P}$ can be studied best in a scheme with fewer $x_{I\!P}$ intervals (two per decade) and an x (or β) and Q^2 binning very similar to that used in inclusive structure function measurements [27]. This also leads naturally to the investigation of the QCD (x, Q^2) structure at fixed $x_{I\!P}$ and to the ratio of diffractive to inclusive cross sections $\sigma_r^D(x_{I\!P}, x, Q^2)/\sigma_r(x, Q^2)$ at fixed $x_{I\!P}$.

2.5 Systematic Uncertainties

A detailed systematic error analysis has been performed in which the sensitivity of the measurement to variations in the efficiencies and energy scales of the detector components and to variations in the details of the Monte Carlo models used for corrections are evaluated.

For this analysis, the energy E'_e and polar angle θ_e of the scattered electron candidate are measured to 1.5% and $0.5\ \mathrm{mrad}$, respectively, the hadronic energy scales of the LAr and SPACAL calorimeters are known to 4% and 7% respectively and the uncertainty in the energy fraction carried by tracks in the hadronic final state algorithm is 3%.

Normalisation uncertainties arise from the uncertainties in the efficiencies of the trigger and the BDC (1% each). The correction factor for diffractive events rejected due to noise in the FMD was varied by 25%. The uncertainty in the luminosity measurement leads to a 2.0% error.

The model dependence of the acceptance and migration corrections is estimated by varying the shapes of the kinematic distributions in the RAPGAP simulation beyond the limits imposed by previous measurements or the present data and by varying the relative normalisations of the different Monte Carlo models used in the acceptance corrections. The background subtracted due to photoproduction (PHOJET) and QED Compton (COMPTON) events was varied by 25%. The use of different approximations for higher order QCD diagrams (the parton shower or the colour dipole approach) leads to an uncertainty of less than 3% in the cross sections. There is an uncertainty of 3% associated with the bin-centre and QED radiative corrections.

A normalisation uncertainty of 6.6% and an uncorrelated uncertainty of 4.9% arises from the correction for smearing about the M_{Y} limit of the measurement. These uncertainties are estimated by variations of the ratio of elastic to proton dissociation cross sections between 1:2 and 2:1, the generated M_{Y} and t distribution in the proton dissociation simulation, the simulated efficiencies of the FMD and PRT detectors by 5% and 25% respectively and the plug energy scale by 30%.

The resulting systematic error is in the range 10-15% for most of the data points, the largest contribution arising from the correction to the measured M_{Y} and t regions. In all figures, the inner error bars on the data points correspond to the statistical error, the outer error bars to the statistical and systematic errors added in quadrature. The combined normalisation error of 6.7% is not shown.

3 The Diffractive Reduced Cross Section

3.1 Comparison with Previous Data

The measured diffractive reduced cross section $\sigma_r^{D(3)}(\beta, Q^2, x_{I\!P})$ is compared with previous H1 data [3] in figure 2. The improved statistics of the new measurement allow the structure function to be extracted in an increased number of Q^2 and $x_{I\!P}$ bins. In the region $Q^2 \geq 15\ \mathrm{GeV}^2$, the statistical precision is considerably improved. The two measurements are in good agreement with the exception of the low β, medium Q^2 region, where the previous data tend to be slightly higher than the new measurement.

Parameter	Value
$\alpha'_{I\!P}$	0.26 ± 0.26 GeV^{-2}
$B_{I\!P}$	$4.6^{+3.4}_{-2.6}$ GeV^{-2}
$\alpha'_{I\!R}$	0.90 ± 0.10 GeV^{-2}
$B_{I\!R}$	2.0 ± 2.0 GeV^{-2}
$\alpha_{I\!R}(0)$	0.50 ± 0.16

Table 1: The parameter values and assumed uncertainties used for the parameterisation of the pomeron and reggeon flux factors.

3.2 Dependence on $x_{I\!P}$ and Effective Pomeron Intercept

The $x_{I\!P}$ dependence of the measured diffractive reduced cross section $\sigma_r^{D(3)}(\beta, Q^2, x_{I\!P})$ for fixed β and Q^2 (figure 2) is studied, following a similar procedure to that adopted in [3]. A fit is performed to the data using a parameterisation of the form

$$\sigma_r^{D(3)}(x_{I\!P}, \beta, Q^2) = f_{I\!P}(x_{I\!P}) A_{I\!P}(\beta, Q^2) + f_{I\!R}(x_{I\!P}) A_{I\!R}(\beta, Q^2) \; , \tag{13}$$

which is motivated by Regge phenomenology. $f_{I\!P}(x_{I\!P})$ and $f_{I\!R}(x_{I\!P})$ correspond to pomeron and sub-leading reggeon *flux factors* and are defined as

$$f_{\{I\!P,I\!R\}}(x_{I\!P}) = \int_{t_{cut}}^{t_{min}} \frac{e^{B_{\{I\!P,I\!R\}} t}}{x_{I\!P}^{2\alpha_{\{I\!P,I\!R\}}(t)-1}} \, \mathrm{d}t \; , \tag{14}$$

where $t_{cut} = -1.0$ GeV^2, $|t_{min}|$ is the minimum kinematically allowed value of $|t|$ and the pomeron and reggeon trajectories are assumed to be linear:

$$\alpha_{\{I\!P,I\!R\}}(t) = \alpha_{\{I\!P,I\!R\}}(0) + \alpha'_{\{I\!P,I\!R\}} t \; . \tag{15}$$

The values for $\alpha'_{I\!P}$, $B_{I\!P}$, $\alpha'_{I\!R}$ and $B_{I\!R}$ cannot be constrained by the $\sigma_r^{D(3)}$ data and are taken from other measurements [20]. Furthermore, the secondary reggeon trajectory intercept $\alpha_{I\!R}(0)$ is not well constrained by the present data due to a lack of high precision data points at high $x_{I\!P}$ (low y) values. It is taken from [3]. The values assumed for the parameterisation of the pomeron and reggeon flux factors are given in table 1.

A fit is performed to all data with $y < 0.45$ in every (Q^2,β) bin of the measurement which contains at least four data points. The cut in y limits the influence of the unmeasured F_L^D, which is taken to be zero by default. The free parameters in the fit are the pomeron intercept parameter $\alpha_{I\!P}(0)$ and the coefficients $A_{I\!P}(\beta, Q^2)$ and $A_{I\!R}(\beta, Q^2)$ in each (β,Q^2) bin. The fit gives a very good description of the data and has a χ^2 per degree of freedom (χ^2/ndf) of 0.95. If the presence of a sub-leading reggeon exchange contribution is neglected, a considerably poorer $\chi^2/\mathrm{ndf} = 1.25$ is obtained.

The experimental systematic error on $\alpha_{I\!P}(0)$ is obtained by repeating the fit after shifting the data points according to each individual source of systematic uncertainty (section 2.5). The fit is also repeated several times with variations in the theoretical assumptions and input parameters, in order to evaluate the model dependence uncertainty. The possibility of interference between the pomeron and reggeon exchange contributions is taken into account by repeating the fit with the assumption of maximal interference, where the interference flux is parameterised as in [3]. The assumed values for $\alpha'_{I\!P}$, $B_{I\!P}$, $\alpha'_{I\!R}$, $B_{I\!R}$ and $\alpha_{I\!R}(0)$ are varied within the limits quoted in table 1. The uncertainty in the size of F_L^D is conservatively taken into account by repeating the fit under the extreme assumption of $F_L^{D(3)} = F_2^{D(3)}$ and taking the difference in the result as an additional model dependence uncertainty.

The result of the fit is

$$\alpha_{I\!P}(0) = 1.173 \ \pm 0.018\,(\mathrm{stat.}) \ \pm 0.017\,(\mathrm{syst.})\ ^{+0.063}_{-0.035}\,(\mathrm{model})\ . \qquad (16)$$

The dominant uncertainty arises from the variation of $F_L^{D(3)}$. The obtained value for the pomeron intercept is significantly higher than the value $\alpha_{I\!P}(0) \simeq 1.08$ for the *soft pomeron* [30] describing soft hadronic interactions. The result is compatible with that obtained from similar fits to previous H1 $F_2^{D(3)}$ data [3].

In order to investigate whether $\alpha_{I\!P}(0)$ has any dependence on Q^2, the fits are repeated with the data divided into two Q^2 intervals covering the ranges $6.5 < Q^2 < 20\ \mathrm{GeV}^2$ and $25 < Q^2 < 120\ \mathrm{GeV}^2$ respectively. The results are

$$\alpha_{I\!P}(0) = 1.162 \ \pm 0.021\,(\mathrm{stat.}) \ \pm 0.018\,(\mathrm{syst.})\ ^{+0.064}_{-0.034}\,(\mathrm{model}) \quad (\langle Q^2\rangle = 10.8\ \mathrm{GeV}^2) \qquad (17)$$

and

$$\alpha_{I\!P}(0) = 1.204 \ \pm 0.034\,(\mathrm{stat.}) \ \pm 0.027\,(\mathrm{syst.})\ ^{+0.060}_{-0.037}\,(\mathrm{model}) \quad (\langle Q^2\rangle = 49.5\ \mathrm{GeV}^2)\ . \qquad (18)$$

Within the uncertainties, there is no evidence for a variation of $\alpha_{I\!P}(0)$ with Q^2 in the measured kinematic range. These results are shown together with the previous H1 measurement in figure 3. The effective pomeron intercept extracted from the diffractive data is also compared with $\alpha_{I\!P}(0) = \lambda + 1$ as obtained from fits of the form $F_2 = cx^{-\lambda(Q^2)}$ to inclusive small x proton structure function data [31]. The data suggest that at large Q^2, the effective intercept describing the inclusive data is larger than that from the diffractive data.

3.3 Dependence on β and Q^2

In order to study the β and Q^2 dependence of the data with high precision, the reduced cross section is extracted at several fixed values of $x_{I\!P}$. In order to illustrate the β and Q^2 dependences in as much detail as possible and to compare the results from different $x_{I\!P}$ bins, the data are presented in figures 4 and 5 in the form $\sigma_r^{D(3)}/f_{I\!P}(x_{I\!P})$, where $f_{I\!P}(x_{I\!P})$ corresponds to the "pomeron flux" used in the Regge and QCD fits (equation 14), with parameters as explained in section 3.2.[3] The data are compared with the results of the NLO DGLAP QCD fit presented in section 5. In order to avoid regions which are most likely to be affected by F_L^D or sub-leading reggeon exchange, only data with $y < 0.6$ and $x_{I\!P} \leq 0.01$ are shown. The "pomeron flux" is used here primarily as a convenient parameterisation of the $x_{I\!P}$ dependence, though the similarity of the normalised reduced cross sections from different $x_{I\!P}$ values in the overlap

[3]The results are presented in detail in in figures A1-A6 in the appendix, where H1 preliminary data for $200 \leq Q^2 \leq 800\ \mathrm{GeV}^2$ [5] are also shown to be consistent with the observed dependence on Q^2 (figure A4).

regions indicates that a factorising $x_{I\!P}$ dependence of the diffractive cross section is a good approximation.

A striking feature of the data is the scaling violations with positive $\partial\sigma_r^{D(3)}/\partial \ln Q^2$ throughout most of the phase space, becoming negative only at the highest measured values of β (figure 5). This behaviour is different from that observed for the scaling violations of $F_2(x, Q^2)$ at fixed x, which are negative for $x \gtrsim 0.1$. In a QCD interpretation, the measured Q^2 dependences are strongly suggestive of a large gluonic component of the diffractive exchange.

The β or x dependences of the reduced cross section at fixed $x_{I\!P}$ and Q^2 (figure 4) are relatively flat and remain large up to the highest possible fractional momenta of $\beta = 1$ or $x = x_{I\!P}$. At the lowest measured Q^2, a rising behaviour of $\sigma_r^{D(3)}$ is observed in the data as $\beta \to 1$, which becomes less pronounced with increasing Q^2. In a leading order QCD picture, the reduced cross section can be viewed as a charge weighted sum over the diffractive quark densities. The β and Q^2 dependences are consistent with DGLAP evolution from high to low β with increasing Q^2 due to gluon radiation.

3.4 Logarithmic Q^2 Derivatives

For (x,$x_{I\!P}$) bins in which there are data points for at least 3 values of Q^2, the logarithmic Q^2 derivative, $B_{\rm D} = \partial\sigma_r^D/\partial \ln Q^2$ is extracted from fits of the form

$$\sigma_r^D = A_{\rm D}(x, x_{I\!P}) + B_{\rm D}(x, x_{I\!P}) \ln Q^2 \ . \tag{19}$$

The logarithmic Q^2 derivative is sensitive to the LO diffractive gluon density convoluted with α_s and the splitting function P_{qg}. The results for $B_{\rm D}$ from these fits are shown in figure 6 for different $x_{I\!P}$ values as a function of β. The logarithmic derivatives have a relatively weak dependence on β for $\beta \lesssim 0.6$. Above this value, the behaviour changes rapidly, with the derivative changing sign in the region of $\beta \sim 0.7$. As expected in Regge factorisation models, the scaling violations at fixed β are very similar at the different $x_{I\!P}$ values, even though the data from different $x_{I\!P}$ values are sensitive to different Q^2 regions.

3.5 Comparison With Models For Diffractive DIS

In this section, several phenomenological models for diffractive DIS are confronted with the data. Comparisons are made for the diffractive structure function $F_2^{D(3)}(\beta, Q^2, x_{I\!P})$, which is extracted from the reduced cross section under the assumption[4] that $F_L^D = 0$.

[4]Since F_L^D only has a non-negligible effect on the measured reduced cross section $\sigma_r^{D(3)}$ at high y values and because of the kinematic range of the present data, this represents a very good approximation in most of the phase space of the measurement.

3.5.1 Semi-classical Model

In figure 7, the Q^2 and β dependences of the diffractive structure function $F_2^{D(3)}(\beta, Q^2, x_{I\!P})$ at fixed $x_{I\!P} = 0.003$ are compared with the "semi-classical" model by Buchmüller, Gehrmann and Hebecker [32]. In this model, DIS is considered in terms of the scattering from the proton of $q\bar{q}$ and $q\bar{q}g$ fluctuations of the virtual photon, modelled as colour dipoles. The partonic fluctuations of the photon scatter from a superposition of colour fields of the proton according to a simple non-perturbative model that averages over all colour field configurations. All resulting final state configurations contribute to the inclusive proton structure function $F_2(x, Q^2)$. Those in which the scattered partons emerge in a net colour-singlet state contribute to the diffractive structure function F_2^D. The model contains only four free parameters, which are obtained from a combined fit to previous F_2 and F_2^D data. The model reproduces the general features of the present measurement, but lies above the data where β and Q^2 are both small. The behaviour of F_2^D in the region of small masses $M_X < 2$ GeV (corresponding to large β), is not expected to be reproduced by the model.

3.5.2 Saturation Model

In figure 8, the data are compared with another colour dipole model by Golec-Biernat and Wüsthoff [33]. In this model, the $q\bar{q}$ and $q\bar{q}g$ dipole cross sections are obtained from fits to F_2 data. The same dipole cross sections are then used to predict $F_2^{D(3)}(\beta, Q^2, x_{I\!P})$ under the assumption of two-gluon exchange, with only one additional free parameter, corresponding to the exponential t dependence of the data, e^{Bt} where $B = 6\ \mathrm{GeV}^{-2}$. Unlike the semi-classical model, the saturation model also contains a higher twist contribution at large β, corresponding to the longitudinal $\gamma^* \rightarrow q\bar{q}_L$ photon fluctuation, allowing comparisons to be made throughout the full measured kinematic region. Relative to the original predictions in [33], an additional colour factor of $(4/9)^2$ has been included for the $q\bar{q}g$ contribution for the current comparisons [34]. The model gives a reasonable description of the data at high and medium β, where the contributions from $q\bar{q}$ fluctuations of longitudinally and transversely polarised photons dominate. With the additional colour factor, the $q\bar{q}g$ fluctuations of transversely polarised photons are insufficient to describe the data in the low β, high Q^2 region.

3.5.3 Soft Colour Interactions

The $x_{I\!P}$ dependence of the measured $F_2^{D(3)}(\beta, Q^2, x_{I\!P})$ at fixed β and Q^2 is compared with two versions of the "Soft Colour Interactions" (SCI) model [35,36] in figure 9. In these models, the hard interaction in diffractive DIS is treated identically to that in inclusive DIS. Diffraction occurs through soft colour rearrangements between the outgoing partons, leaving their momentum configuration unchanged. In the original SCI model [35], diffractive final states are produced using only one free parameter, the universal colour rearrangement probability, which is fixed by a fit to previous $F_2^{D(3)}$ data. The model has been refined [36] by making the colour rearrangement probability proportional to the normalised difference in the generalised areas of the string configurations before and after the rearrangement.

The kinematic region shown in figure 9 is restricted to $M_X > 2$ GeV, corresponding to the region for which the model is intended. The model predictions were obtained using the LEPTO $6.5.2\beta$ [37] Monte Carlo generator. The version of SCI based on the generalised area law [36] results in a better description of $F_2^{D(3)}(\beta, Q^2, x_{I\!P})$ at low Q^2 than the original version in [35], with the exception of the highest β region.

4 The Ratio of the Diffractive to the Inclusive Cross Section

The ratio

$$\left. \frac{\sigma_r^D(x_{I\!P}, x, Q^2)}{\sigma_r(x, Q^2)} \right|_{x_{I\!P}} \tag{20}$$

of the diffractive to the inclusive DIS reduced cross sections is extracted at fixed $x_{I\!P}$ in order to compare the dynamics of diffractive DIS with those of inclusive DIS. The values of $\sigma_r(x, Q^2)$ are taken from [27]. The ratio as a function of Q^2, shown for all $x_{I\!P}$ bins in figure 10,[5] tests the difference between the scaling violations of σ_r^D and σ_r when compared at the same x. At low values of β (or x), the ratio is remarkably flat as a function of Q^2 for all $x_{I\!P}$ values. At the highest β, where x approaches $x_{I\!P}$, the ratio falls with increasing Q^2.

In order to quantify the differences between the Q^2 dependences of σ_r^D and σ_r at fixed x and $x_{I\!P}$, the logarithmic derivative $B_{\mathrm{R}}(x, x_{I\!P})$ of the ratio is extracted from fits of the form

$$\left. \frac{\sigma_r^D(x_{I\!P}, x, Q^2)}{\sigma_r(x, Q^2)} \right|_{x, x_{I\!P}} = A_{\mathrm{R}}(x, x_{I\!P}) + B_{\mathrm{R}}(x, x_{I\!P}) \ln Q^2 \; . \tag{21}$$

The resulting values of B_{R} are shown in figure 11 with the "pomeron flux" $f_{I\!P/p}$ (equation 14) divided out, so that the results at different $x_{I\!P}$ can be compared in normalisation as well as shape. The Q^2 dependences of the diffractive and inclusive cross sections are consistent with being the same away from $x = x_{I\!P}$ ($\beta = 1$), suggesting that the ratio of the diffractive gluon density of the proton to the total gluon density is approximately constant in this region. This behaviour is expected in models in which rapidity gap formation is a purely probabilistic mechanism, for example due to multiple soft rearrangements of colour configurations [35]. In dipole models, for which the diffractive cross section is proportional to the dipole cross section squared and the inclusive cross section depends linearly on the dipole cross section, this behaviour can be reproduced provided that the dipole cross section grows with increasing dipole size [32,33,38]. As $\beta \rightarrow 1$, the logarithmic Q^2 derivative at fixed x becomes negative for all $x_{I\!P}$. This may suggest that the high β region of diffraction is driven by perturbative 2-gluon exchange [39], which is inherently higher twist and thus leads to a suppression with increasing Q^2. However, this behaviour also occurs naturally in resolved pomeron models, in which gluon radiation shifts the β dependence to lower values as Q^2 increases. At fixed β, there is no significant dependence of the logarithmic derivative on $x_{I\!P}$.

The ratio as a function of x with Q^2 and $x_{I\!P}$ fixed is shown in figure 12. For each $x_{I\!P}$, dashed lines indicate the points in x at which $\beta = 1$ ($x = x_{I\!P}$). Dotted lines indicate the point

[5] The results are shown separately for each $x_{I\!P}$ and x bin in figure A7 in the appendix.

where $\beta = 0.1$ ($x = 0.1 \cdot x_{I\!P}$). For $\beta > 0.1$, a complicated structure is observed in the ratio, corresponding to the high β behaviour of σ_r^D (see figure 4). For $\beta < 0.1$, there is a suggestion that a flatter dependence develops, though there are limited data in this region.

A different approach to presenting the ratio of the diffractive to the inclusive cross sections is to extract the quantity $\rho^{D(3)}$, defined as

$$\rho^{D(3)} = M_{\rm X}^2 \frac{{\rm d}\sigma(\gamma^* p \to XY)}{{\rm d}M_{\rm X}^2} \; / \; \sigma(\gamma^* p \to X) = \frac{M_{\rm X}^2 \, x}{Q^2} \cdot \frac{\sigma_r^{D(3)}(\beta, Q^2, x_{I\!P})}{\sigma_r(x, Q^2)} \,, \quad (22)$$

This ratio is shown in figure 13 as a function of W in bins of fixed Q^2 and β. $\rho^{D(3)}$ is relatively flat throughout the full phase space, except at large β values (the very low $M_{\rm X}$ region) and at low W (high $x_{I\!P}$), where sub-leading reggeon exchange becomes important. When studying the W (or x) dependence at fixed Q^2 and β, $M_{\rm X}$ is held fixed, as was the case in [4, 7]. By contrast, in the ratio defined by equation (20), $x_{I\!P}$ and Q^2 are held fixed as x varies, such that $M_{\rm X}^2 = Q^2(x_{I\!P}/x - 1)$ also varies with x.

5 Next-to-leading Order DGLAP QCD Fit

Leading (LO) and next-to-leading order (NLO) QCD fits have been performed to the diffractive reduced cross section $\sigma_r^{D(3)}(\beta, Q^2, x_{I\!P})$ to determine diffractive parton distributions (dpdfs) and to test QCD hard scattering factorisation. The data used in the fit are restricted to $M_X > 2$ GeV to justify a leading twist approach. The NLO fit is performed to the reduced cross section σ_r^D. The effects of F_L^D are considered through its relation to the NLO gluon density such that no explicit cut on y is required. For the LO fit, an additional cut $y < 0.45$ is applied to reduce any possible effect of F_L^D to a negligible level.[6] In addition to the data from the present analysis (284 points), H1 preliminary data at higher Q^2 [5], covering $200 \leq Q^2 \leq 800$ GeV^2 are included (29 points).

5.1 QCD Fit Technique

In the fit, the shape of the dpdfs is assumed to be independent of $x_{I\!P}$ ("Regge factorisation", equation 8), which is supported by the data (figures 4,5). The $x_{I\!P}$ dependence is parameterised according to equations (14,15), using the values of the parameters given in table 1. The value of $\alpha_{I\!P}(0) = 1.173$ is taken from the result of the fit to the $x_{I\!P}$ dependence of the data (equation 16). A sub-leading exchange contribution is included in the fit with parton densities taken from a parameterisation of the pion [40]. Since the sub-leading contribution is negligible except at the highest $x_{I\!P} > 0.01$ values, choosing a different parameterisation [41], does not significantly affect the results.

The diffractive exchange is modelled in terms of a light flavour singlet[7]

$$\Sigma(z) = u(z) + d(z) + s(z) + \bar{u}(z) + \bar{d}(z) + \bar{s}(z) \quad (23)$$

[6] At LO QCD, $F_L^D = 0$.

[7] $u = d = s = \bar{u} = \bar{d} = \bar{s}$ is assumed.

and a gluon distribution $g(z)$ at a starting scale $Q_0^2 = 3\ \mathrm{GeV}^2$. Here, z is the momentum fraction of the parton entering the hard sub-process with respect to the diffractive exchange, such that for the lowest-order quark parton model process $z = \beta$, whereas for higher order processes $0 < \beta < z$. The dpdfs are parameterised using the form

$$zp_i(z, Q_0^2) = \left[\sum_{j=1}^{n} C_j^i P_j(2z-1) \right]^2 e^{\frac{a}{z-1}} \ , \tag{24}$$

where, $P_j(\xi)$ is the j^{th} member of a set of Chebychev polynomials[8]. The series is squared to ensure positivity. The additional exponential term is used to guarantee that in the limit of $z \to 1$, the dpdfs tend to zero. The parameter a is set to 0.01. Leaving out the exponential term results in slight variations of the shape of the extracted dpdfs at the highest $z > 0.95$, which are well within the quoted uncertainties. No momentum sum rule is imposed. Charm quarks are treated in the massive scheme (appearing via boson gluon fusion processes) with $m_c = 1.5 \pm 0.1$ GeV. The strong coupling is set via $\Lambda_{\mathrm{QCD}}^{\overline{\mathrm{MS}}} = 200 \pm 30\ \mathrm{MeV}$.

The LO or NLO DGLAP equations are used to evolve the dpdfs to $Q^2 > Q_0^2$ using the method of [27], extended for diffraction. In the fit, the statistical and the experimental systematic errors of the data points and their correlations [9] are propagated to obtain error bands for the resulting dpdfs [42]. The χ^2 is computed as

$$\chi^2 = \sum_{ij} \frac{\left[\sigma_{ij}^{exp} - \sigma_{ij}^{th}(1 - \nu_j\delta_j - \sum_k c_{jk}\delta_{sys,ijk})\right]^2}{[\sigma_{ij}^{exp}]^2(\delta_{stat,ij}^2 + \delta_{unc,ij}^2)} + \sum_{jk} c_{jk}^2 + \sum_j \nu_j^2 \ , \tag{25}$$

where the indices correspond to data point i of data set j and k counts the individual sources of correlated error. σ_{ij}^{exp} and σ_{ij}^{th} are the measured and calculated cross sections, $\delta_{stat,ij}$ and $\delta_{unc,ij}$ are the relative statistical and uncorrelated systematic errors of the measurements and $\delta_{sys,ijk}$ corresponds to the relative correlated systematic error for a given error source k. The systematics and normalisation parameters c_{jk} and ν_j, which have zero mean and unit variance, are determined by the fit.

A theoretical error in the extracted dpdfs is estimated by variations of Λ_{QCD} and m_c within the limits quoted above and of the parameterisation of the $x_{I\!P}$ dependences by varying the value of $\alpha_{I\!P}(0)$ within its statistical error and the other parameters in the flux factors within the uncertainties quoted in table 1. No theoretical uncertainty is assigned for the choice of parton parameterisation, though the results are consistent within the quoted uncertainties if alternative approaches [43] are used.

The numbers of terms in the polynomial parameterisations used in the fit have been systematically optimised to the precision of the data. For the quark singlet as well as the gluon distributions, the first three terms in the series of polynomials are used, yielding 3 free parameters (C_j^Σ and C_j^g) for each of the singlet and gluon distributions. The normalisation of the sub-leading exchange contribution at high $x_{I\!P}$ is also determined by the fit such that the total number of free parameters is 7. The χ^2 for the central NLO fit is 308.7 for 306 degrees of freedom.

[8] $P_1 = 1$, $P_2 = \xi$ and $P_{j+1}(\xi) = 2\xi P_j(\xi) - P_{j-1}(\xi)$.

[9] The systematic errors of the high Q^2 measurement [5] are taken to be fully uncorrelated.

5.2 Comparison of the NLO Fit with Data

The result of the fit is compared with the present data in figures 4, 5 and A1-A6. A comparison with the higher Q^2 data [5] is shown in figure A8. The fit reproduces the features of the data very well, in particular the rising behaviour of $\sigma_r^{D(3)}$ towards $\beta \rightarrow 1$ at low Q^2 (figure 4) and the rising scaling violations which persist up to high β values (figure 5). In figures A1-A3, the size of the sub-leading exchange contribution as determined by the fit is also displayed. It only plays a significant role for $x_{I\!P} \geq 0.01$. Compared with previous H1 results [3], its normalisation is reduced by approximately 50%.

5.3 Diffractive Parton Distributions

The dpdfs resulting from the NLO QCD fit are presented in figures 14 and 15. The inner error bands correspond to the experimental error and the outer error bands to the experimental and theoretical errors added in quadrature. The quark singlet as well as the gluon distribution extend to large fractional momenta z. Whereas the singlet distribution is well constrained by the fit, there is a substantial uncertainty in the gluon distribution at $z > 0.5$, mainly due to the model assumptions. At smaller z, the relative size of the uncertainties is significantly reduced.

The shape of the singlet distribution is a direct consequence of the shape of the observed β distribution in the reduced cross section, whereas the gluon distribution is determined mainly through the scaling violations. As was the case in previous QCD fits to diffractive DIS data, the gluon distribution is much bigger than the quark distribution, showing that the diffractive exchange is mediated dominantly by gluons. The fraction of the exchanged momentum carried by gluons is quantified in terms of the ratio

$$\frac{\int \mathrm{d}z \; g(z,Q^2)}{\int \mathrm{d}z \; \Sigma(z,Q^2) + \int \mathrm{d}z \; g(z,Q^2)} \, ,$$

integrated over the measured region $0.01 < z < 1$. This fraction is shown as a function of Q^2 in figure 16. The integrated fraction of the exchanged momentum carried by gluons is $\sim 75 \pm 15\%$ (total error), which is fully consistent with earlier results [3].

The central values from the LO fit are also shown in figures 14 and 15. The LO gluon density shows a peak at the highest z. This peak disappears for the central values when moving to NLO. The LO results are compared with the previous H1 QCD fits to older F_2^D data [3] in figure 17. The central values of the singlet distributions agree reasonably well between the previous and the new fits. The shape of the new gluon distribution is similar to that from 'H1 fit 3', except that the peak at the highest z is significantly reduced.[10] The normalisation is different by about 30% at low to medium z. The uncertainties in the LO dpdfs derived from the present data are similar to those in the NLO dpdfs (figure 15). The errors on the 'H1 fit 2 / 3' parton distributions are significantly larger, especially for the gluon distribution. Taking these uncertainties into account, the old and the new parton distributions are in agreement.

[10] The functional flexibility of the 'fit 2' gluon distribution is limited since the parameterisation allows for no more than a constant dependence on z at Q_0^2.

5.4 The Longitudinal Structure Function F_L^D

At NLO in QCD, the leading twist component of the longitudinal diffractive structure function F_L^D is given by

$$\frac{F_L^D}{z} \sim \frac{\alpha_s}{2\pi}\left[C_q^L \otimes \bar{F}_2^D + C_g^L \otimes \sum_i e_i^2\, g^D\right] , \tag{26}$$

where $\bar{F}_2^D = \sum_i e_i^2[q_i^D + \bar{q}_i^D]$, C_q and C_g are Wilson coefficients, e_i is the charge of quark species i and $\otimes$ represents a convolution integral. Figure 18 shows the prediction for F_L^D from the NLO fit as a function of β and Q^2 at fixed $x_{I\!P} = 0.003$. The longitudinal structure function increases relative to F_2^D towards low Q^2 and β. The values of F_L^D are relatively large, due to their relation to the gluon density.

In figures A1-A6, the prediction of the NLO QCD fit for the diffractive reduced cross section $\sigma_r^{D(3)}$ under the assumption that $F_L^D = 0$ is also shown. The effect of a non-zero F_L^D is a taming of the rise of the cross section towards low β or x (high y) at fixed $x_{I\!P}$ and Q^2. The effects of F_L^D are constrained to the limits of the acceptance of the present measurement, such that the direct sensitivity is weak.

6 Factorisation Tests With Hadronic Final State Observables

QCD factorisation in diffraction can be tested by taking the dpdfs extracted from σ_r^D in DIS (see previous section) and predicting diffractive final state observables such as dijet and charm cross sections at HERA. Both of these processes are highly sensitive to the diffractive gluon distribution via the boson-gluon fusion process $\gamma^* g \rightarrow q\bar{q}$. Predictions can also be made for hard diffractive processes in hadron-hadron interactions, for example diffractive dijet production at the Tevatron. In the following, the LO diffractive parton distributions described in section 5 are used for these comparisons.

6.1 Diffractive Jet and Charm Production at HERA

Predictions for diffractive DIS jet and charm production cross sections are obtained using the RAPGAP [21] Monte Carlo program and are made at the level of stable hadrons. The renormalisation and factorisation scales are set to $\mu^2 = Q^2 + p_T^2 + m_q^2$. In figure 19, comparisons are made between the new dpdfs and H1 measurements of diffractive dijet [11] and D^* meson [12] cross sections differential in hadron level estimators of $z_{I\!P}$. For comparison, predictions based on the previous H1 QCD fits ('H1 fit 2 and 3' in [3]) are also shown. The predictions based on the QCD fit to the present data are generally below those of the previous fits, due to the reduced normalisation of the diffractive gluon distribution. This leads to an improved description of the magnitude of the D^* cross section, but a worse description for that of the dijet cross section. The shapes of both $z_{I\!P}$ distributions are well described by the predictions based on the new dpdfs. The uncertainties in the diffractive parton distributions have not yet been propagated to the final state cross section predictions, though they are expected to be substantial. Higher order QCD corrections are also not fully included in the LO simulation. At the present stage, there is thus no evidence for any breakdown of QCD hard scattering factorisation in diffractive DIS [8].

Further comparisons with diffractive dijet cross sections are shown in the appendix in figures A9-A12. A comparison with a measurement of 3-jet production in diffractive DIS is shown in figure A13. Additional comparisons with diffractive D^* production cross sections are shown in figure A14.

6.2 Diffractive Dijet Production at the Tevatron

The CDF collaboration has made measurements of diffractive dijet production in the process $p\bar{p} \to pX$ collisions at $\sqrt{s} = 1800$ GeV [13]. The results are presented in terms of an *effective diffractive structure function* $\tilde{F}^D_{jj}$ for dijet events, corresponding in resolved pomeron models to

$$\tilde{F}^D_{jj}(\beta, \mu^2) \;=\; \left\{ \beta\, g(\beta, \mu^2) + \frac{4}{9}\, \beta\, q(\beta, \mu^2) \right\} \otimes\; f_{I\!P/p}(x_{I\!P})\;, \tag{27}$$

where μ is the average scale of the measurement, $f_{I\!P/p}(x_{I\!P})$ is the pomeron flux and $\otimes$ represents a convolution of the flux factor with the effective parton densities $g(\beta, \mu^2) + 4/9\; q(\beta, \mu^2)$.

Figure 20 shows a comparison of the CDF measurement with a prediction based on the new diffractive parton distributions, obtained by integrating the dpdfs over the appropriate range $0.035 < x_{I\!P} < 0.95$, $|t| < 1\ \mathrm{GeV}^2$ and taking $\mu^2 = 75\ \mathrm{GeV}^2$, corresponding to the average squared transverse jet energy in the CDF measurement. The new prediction is slightly closer to the data than that using the parton distributions based on the fits to the previous data. However, a discrepancy at the level of an order of magnitude remains. The discrepancy appears to be less dependent on β when the new dpdfs are used. The new QCD fit thus confirms the serious breakdown of factorisation observed when comparing hard diffraction results from ep and $\bar{p}p$ data. This has often been interpreted as being due to additional spectator interactions [44].

7 Summary

A high precision measurement of the inclusive cross section for the diffractive (DIS) process $ep \to eXY$ has been presented, obtained using data taken with the H1 detector at HERA, corresponding to an integrated luminosity of $\mathcal{L} = 10.6\ \mathrm{pb}^{-1}$, a factor five more than previous measurements.

The $x_{I\!P}$ dependence of the data is interpreted in terms of a measurement of the effective pomeron intercept $\alpha_{I\!P}(0)$. The resulting value $\alpha_{I\!P}(0) = 1.173\ \pm 0.018\ (\mathrm{stat.})\ \pm 0.017\ (\mathrm{syst.})\ ^{+0.063}_{-0.035}\ (\mathrm{model})$ confirms previous observations that the energy dependence of diffractive DIS is stronger than that of soft hadronic diffraction. There is no significant variation of the β and Q^2 dependence of the data when $x_{I\!P}$ changes, supporting the hypothesis of Regge factorisation.

The Q^2 dependence at fixed β and $x_{I\!P}$ displays rising scaling violations for $\beta \lesssim 0.7$, with a clear change to a falling behaviour with increasing Q^2 at the highest β. The β dependence of the data is relatively flat, though a clear rise with increasing β is observed at the highest β and low Q^2.

The ratio of the diffractive to the inclusive cross section $\sigma_r^{D(3)}(x, Q^2, x_{I\!P})/\sigma_r(x, Q^2)$ is found to be remarkably flat as a function of Q^2 with $x_{I\!P}$ and x fixed, except at the highest values of β (x approaching $x_{I\!P}$), where the diffractive cross section falls faster than the inclusive.

A NLO DGLAP QCD fit is performed to the data and an assessment is made of the experimental and theoretical uncertainties on the resulting diffractive parton densities. The results confirm that the diffractive exchange is dominated by the gluon density, which remains large up to high fractional momenta. The fraction of the diffractive exchange carried by gluons is found be $(75 \pm 15)\%$ at $Q^2 = 10\ \mathrm{GeV}^2$.

The extracted diffractive parton densities are used to make updated comparisons with diffractive final state measurements. Dijet and open charm cross sections at HERA are found to be well described, whereas a discrepancy of approximately an order of magnitude is observed in the predictions of dijet cross sections from the Tevatron.

Acknowledgements

We are grateful to the HERA machine group whose outstanding efforts have made and continue to make this experiment possible. We thank the engineers and technicians for their work in constructing and now maintaining the H1 detector, our funding agencies for financial support, the DESY technical staff for continual assistance, and the DESY directorate for the hospitality which they extend to the non DESY members of the collaboration.

References

[1] UA8 Collaboration, A. Brandt *et al.*, *Phys. Lett.* **B 297** (1992) 417.

[2] ZEUS Collaboration, M. Derrick *et al.*, *Phys. Lett.* **B 315** (1993) 481.
H1 Collaboration, T. Ahmed *et al.*, *Nucl. Phys.* **B 429** (1994) 477.

[3] H1 Collaboration, C. Adloff *et al.*, *Z. Phys.* **C 76** (1997) 613.

[4] ZEUS Collaboration, J. Breitweg *et al.*, *Eur. Phys. J.* **C 6** (1999) 43.

[5] H1 Collaboration, contributed paper no. 571 subm. to ICHEP 1998 (Vancouver).

[6] H1 Collaboration, *'Measurement of the diffractive structure function $F_2^{D(3)}$'*. Paper submitted to International Europhysics Conference on High Energy Physics EPS01, Budapest, July 2001 (abstract 808). Available from http://www-h1.desy.de/h1/www/publications/htmlsplit/H1prelim-01-111.long.html

[7] ZEUS Collaboration, S. Chekanov *et al.*, DESY-02-029, to appear in *Eur. Phys. J.* **C**

[8] J. Collins, *Phys. Rev.* **D 57** (1998) 3051 and erratum-ibid. **D 61** (2000) 019902.

[9] L. Trentadue, G. Veneziano, *Phys. Lett.* **B 323** (1994) 201;
A. Berera, D. Soper, *Phys. Rev.* **D 50** (1994) 4328;
M. Grazzini, L. Trentadue, G. Veneziano, *Nucl. Phys.* **B 519** (1998) 394.

[10] V. Gribov, L. Lipatov, *Sov. J. Nucl. Phys.* **15** (1972) 438 and 675;
Y. Dokshitzer, *Sov. Phys. JETP* **46** (1977) 641;
G. Altarelli, G. Parisi, *Nucl. Phys.* **B 126** (1977) 298.

[11] H1 Collaboration, C. Adloff *et al.*, *Eur. Phys. J.* **C 20** (2001) 29.

[12] H1 Collaboration, C. Adloff *et al.*, *Phys. Lett.* **B 520** (2001) 191.

[13] CDF Collaboration, T. Affolder *et al.*, *Phys. Rev. Lett.* **84** (2000) 5043.

[14] J. Blümlein and D. Robaschik. *Phys. Rev.* **D 65** (2002) 096002.

[15] G. Ingelman, P. Schlein, *Phys. Lett.* **B 152** (1985) 256.

[16] ZEUS Collaboration, J. Breitweg *et al.*, *Eur. Phys. J.* **C 5** (1998) 41.

[17] L. Alvero, J. C. Collins, J. Terron and J. J. Whitmore, *Phys. Rev.* **D 59** (1999) 074022.

[18] C. Royon, L. Schoeffel, J. Bartels, H. Jung and R. Peschanski, *Phys. Rev.* **D 63** (2001) 074004.

[19] H1 Collaboration, I. Abt *et al.*, *Nucl. Instrum. Methods* **A 386** (1997) 310 and 348.

[20] H1 Collaboration, C. Adloff *et al.*, *Z. Phys.* **C 74** (1997) 221.

[21] H. Jung, *Comp. Phys. Commun.* **86** (1995) 147.
(see also http://www.desy.de/∼jung/rapgap.html)

[22] M. Bengtsson, T. Sjöstrand, *Z. Phys.* **C 37** (1988) 465.

[23] T. Sjöstrand, *Comp. Phys. Commun.* **82** (1994) 74.

[24] A. Kwiatkowski, H. Spiesberger, H. Möhring, *Comp. Phys. Commun.* **69** (1992) 155.

[25] B. List: *Diffraktive J/ψ-Produktion in Elektron-Proton-Stößen am Speicherring HERA*, Diploma Thesis, Tech. Univ. Berlin (1993), unpublished;
B. List, A. Mastroberardino: *DIFFVM: A Monte Carlo Generator for diffractive processes in ep scattering* in *Monte Carlo Generators for HERA Physics*, A. Doyle, G. Grindhammer, G. Ingelman, H. Jung (eds.), DESY-PROC-1999-02 (1999) 396.

[26] G. Schuler and H. Spiesberger, Proc. of the Workshop on Physics at HERA, Vol. 3, eds. W. Buchmüller and G. Ingelman, Hamburg, DESY (1992), p. 1419.

[27] H1 Collaboration, C. Adloff *et al.*, *Eur. Phys. J.* **C 21** (2001) 33.

[28] A. Courau *et al.*, Proc. of the Workshop on Physics at HERA, Vol. 2, eds. W. Buchmüller and G. Ingelman, Hamburg, DESY (1992), p. 902.

[29] R. Engel and J. Ranft, *Phys. Rev.* **D 54** (1996) 4244.

[30] A. Donnachie, P. Landshoff, *Phys. Lett.* **B 296** (1992) 227;
J. Cudell, K. Kang, S. Kim, *Phys. Lett.* **B 395** (1997) 311.

[31] H1 Collaboration, C. Adloff *et al.*, *Phys. Lett.* **B 520** (2001) 183.

[32] W. Buchmüller, T. Gehrmann, A. Hebecker, *Nucl. Phys.* **B 537** (1999) 477.

[33] K. Golec-Biernat, M. Wüsthoff, *Phys. Rev.* **D 59** (1999) 014017;
K. Golec-Biernat, M. Wüsthoff, *Phys. Rev.* **D 60** (1999) 114023;
J. Bartels, K. Golec-Biernat, H. Kowalski, *Phys. Rev.* **D 66** (2002) 014001.

[34] K. Golec-Biernat, private communication.

[35] A. Edin, G. Ingelman, J. Rathsman, *Phys. Lett.* **B 366** (1996) 371;
A. Edin, G. Ingelman, J. Rathsman, *Z. Phys.* **C 75** (1997) 57.

[36] J. Rathsman, *Phys. Lett.* **B 452** (1999) 364.

[37] A. Edin, G. Ingelman, J. Rathsman, *Comp. Phys. Commun.* **101** (1997) 108.

[38] M. McDermott, L. Frankfurt, V. Guzey, M. Strikman, *Eur. Phys. J.* **C 16** (2000) 641.

[39] A. Hebecker, T. Teubner, *Phys. Lett.* **B 498** (2001) 16.

[40] J. Owens, *Phys. Rev.* **D 30** (1984) 943.

[41] M. Glück, E. Reya and A. Vogt, *Z. Phys.* **C 53** (1992) 651.

[42] C. Pascaud, F. Zomer, Preprint LAL-95-05.

[43] A. Martin, R. Roberts, W. Stirling, R. Thorne, *Phys. Lett.* **B 531** (2002) 216.

[44] J. Bjorken, *Phys. Rev.* **D 47** (1993) 101.

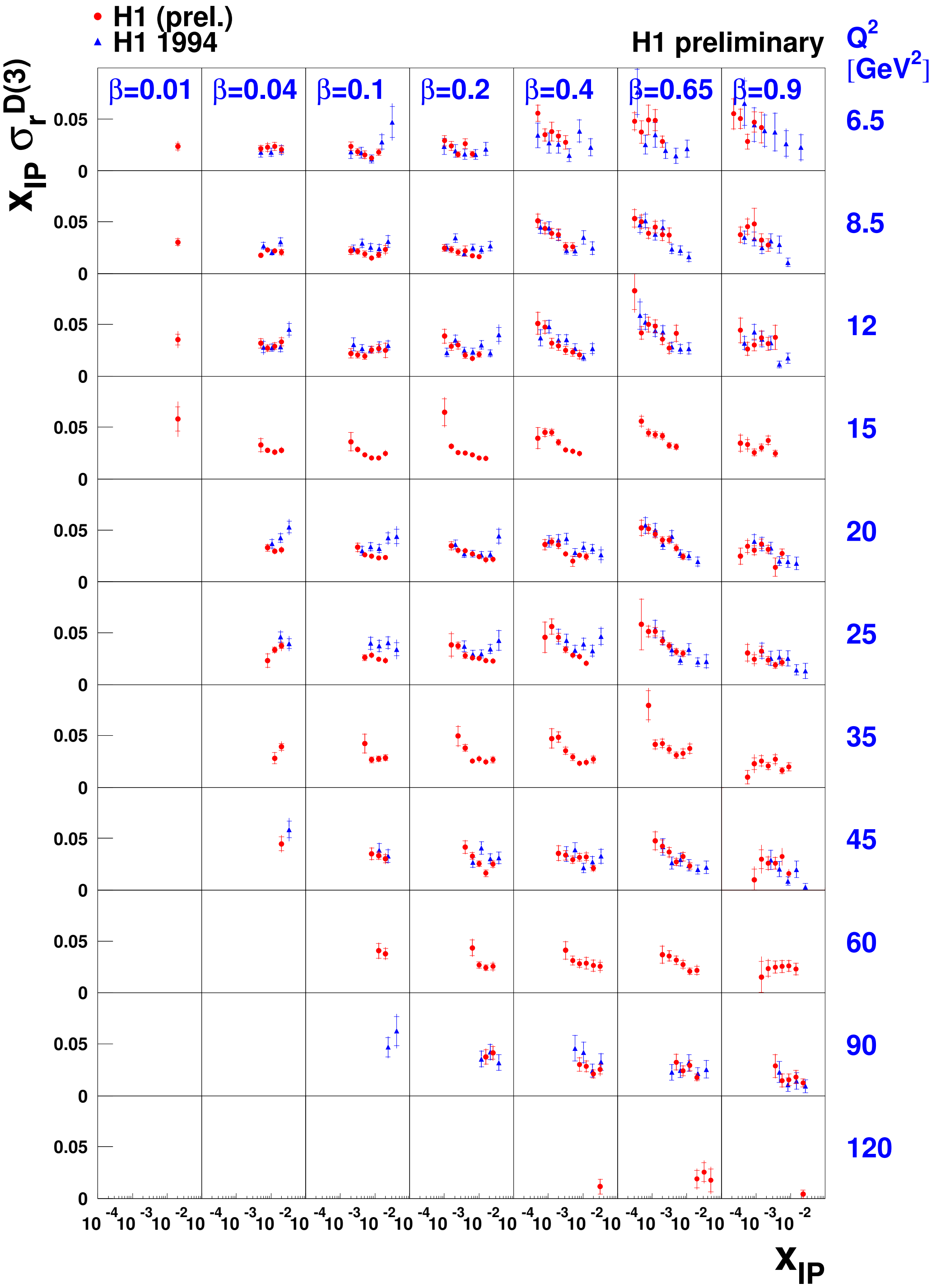

Figure 2: The measured diffractive reduced cross section *(filled circles)*, presented as $x_{I\!P}\sigma_r^{D(3)}$ and plotted as a function of $x_{I\!P}$ at fixed values of β and Q^2. Here and in all other figures, the inner error bars correspond to the statistical error, the outer error bars show the statistical and the systematic error added in quadrature. An additional normalisation uncertainty of 6.7% is not shown. For comparison, the previous H1 measurement in [3] is also shown *(triangles)*.

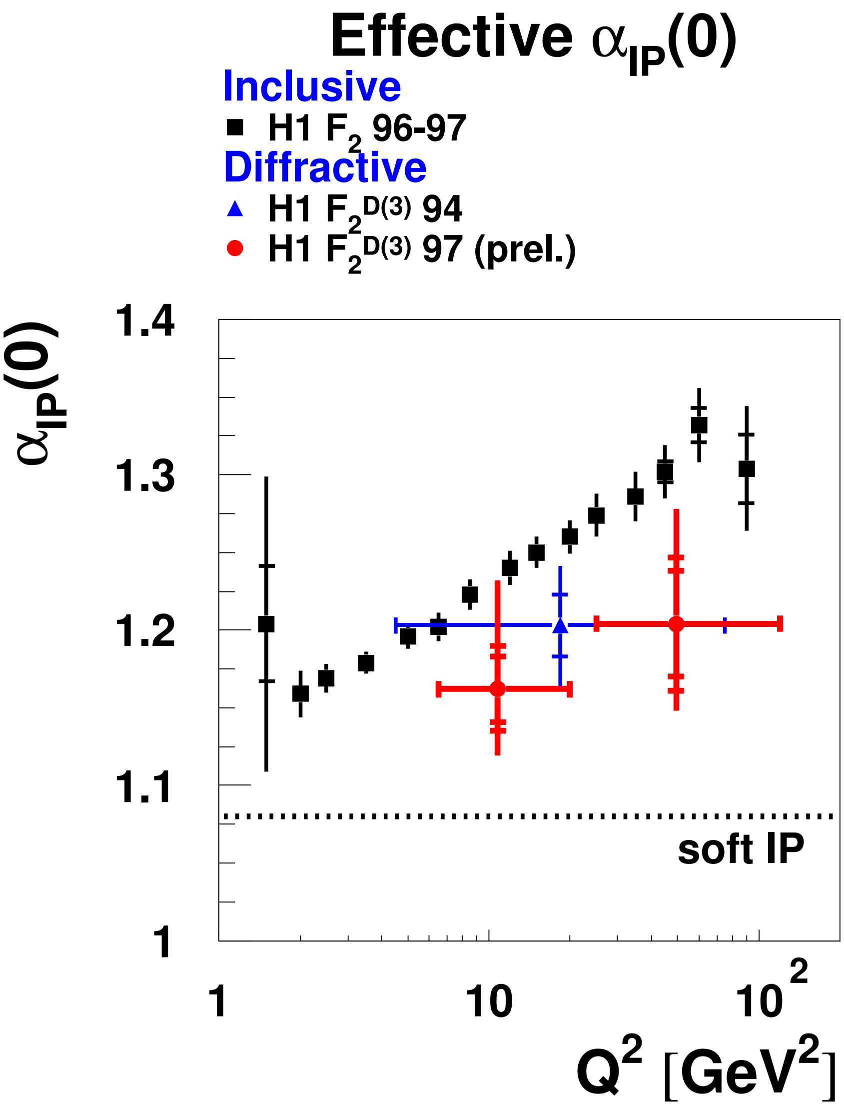

Figure 3: The effective value of $\alpha_{\mathbb{P}}(0)$ as a function of Q^2. The squares correspond to $\alpha_{\mathbb{P}}(0) = 1+\lambda$ extracted from a fit $F_2 = cx^{-\lambda(Q^2)}$ to inclusive $F_2(x, Q^2)$ data [31] for $x < 0.01$. The filled circles are the values of $\alpha_{\mathbb{P}}(0)$ as obtained from the phenomenological Regge fit to the $\sigma_r^{D(3)}$ data as described in the text, for two different Q^2 intervals. The inner error bars correspond to the statistical errors. The middle error bars show the statistical and experimental systematic errors added in quadrature. The outer error bars show the full error, including that arising from model dependence. The triangle is the value of $\alpha_{\mathbb{P}}(0)$ obtained in [3].

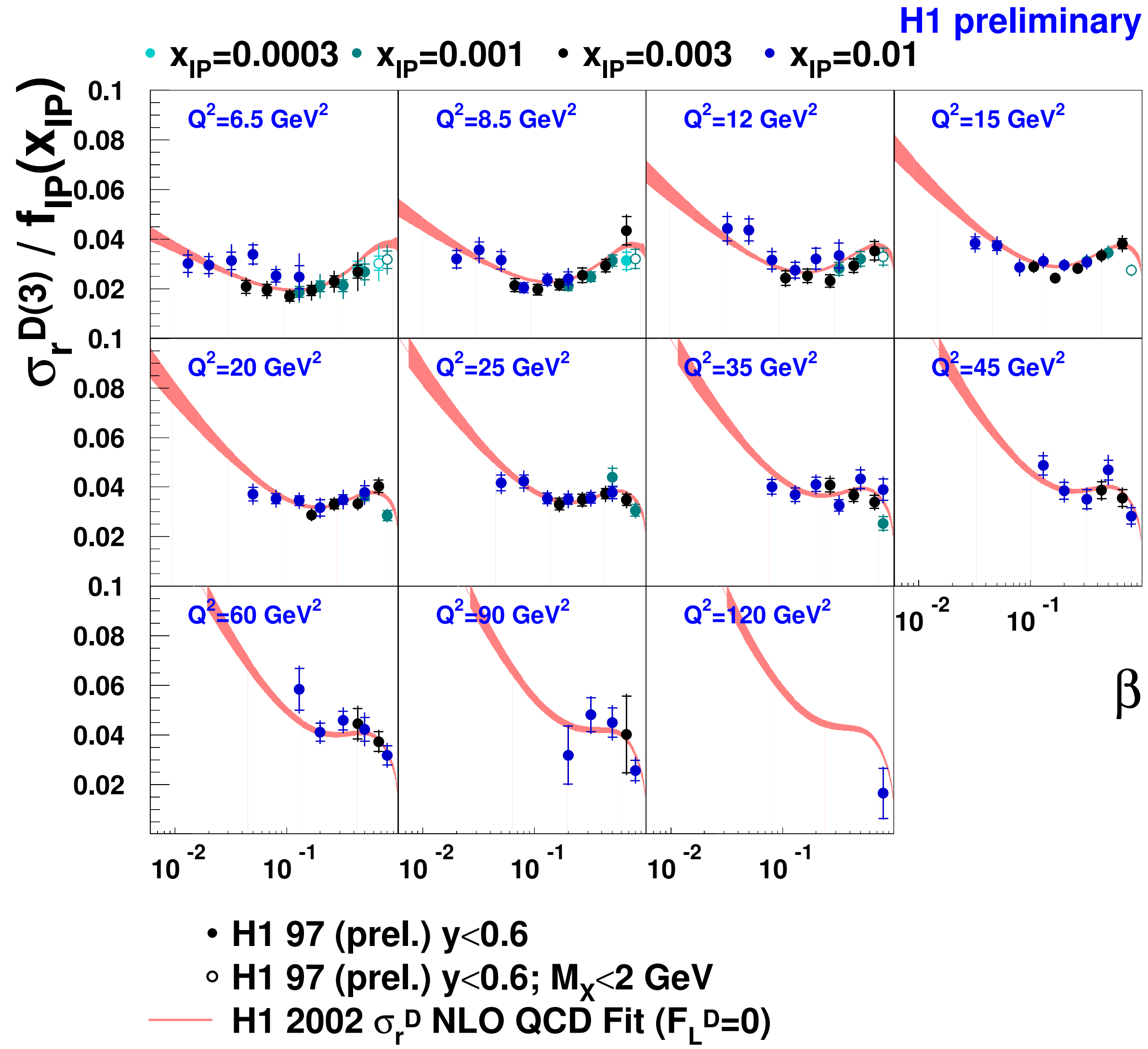

Figure 4: β dependence of the reduced cross section scaled at each $x_{I\!P}$ by the values assumed for the t-integrated pomeron flux in the QCD fits (equation 14). Only data with $y < 0.6$ are shown to minimise the influence of the longitudinal structure function F_L^D. The data are compared with the prediction of the NLO QCD fits (experimental errors only) under the assumption that $F_L^D = 0$.

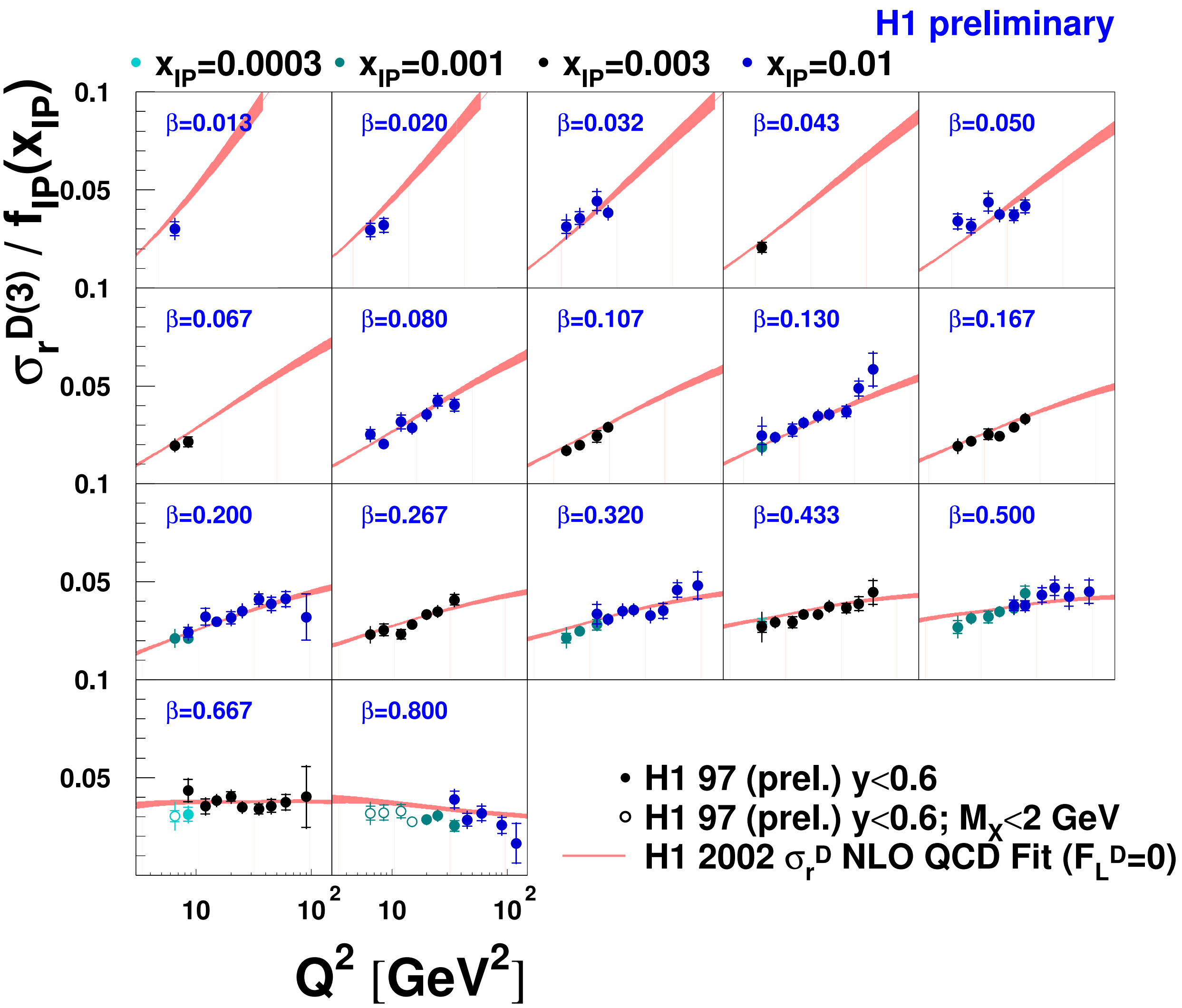

Figure 5: Q^2 dependence of the reduced cross section ($y < 0.6$) scaled at each $x_{I\!P}$ by the values assumed for the t-integrated pomeron flux in the QCD fits (equation 14). The data are compared with the prediction of the NLO QCD fits (experimental errors only) for $F_L^D = 0$.

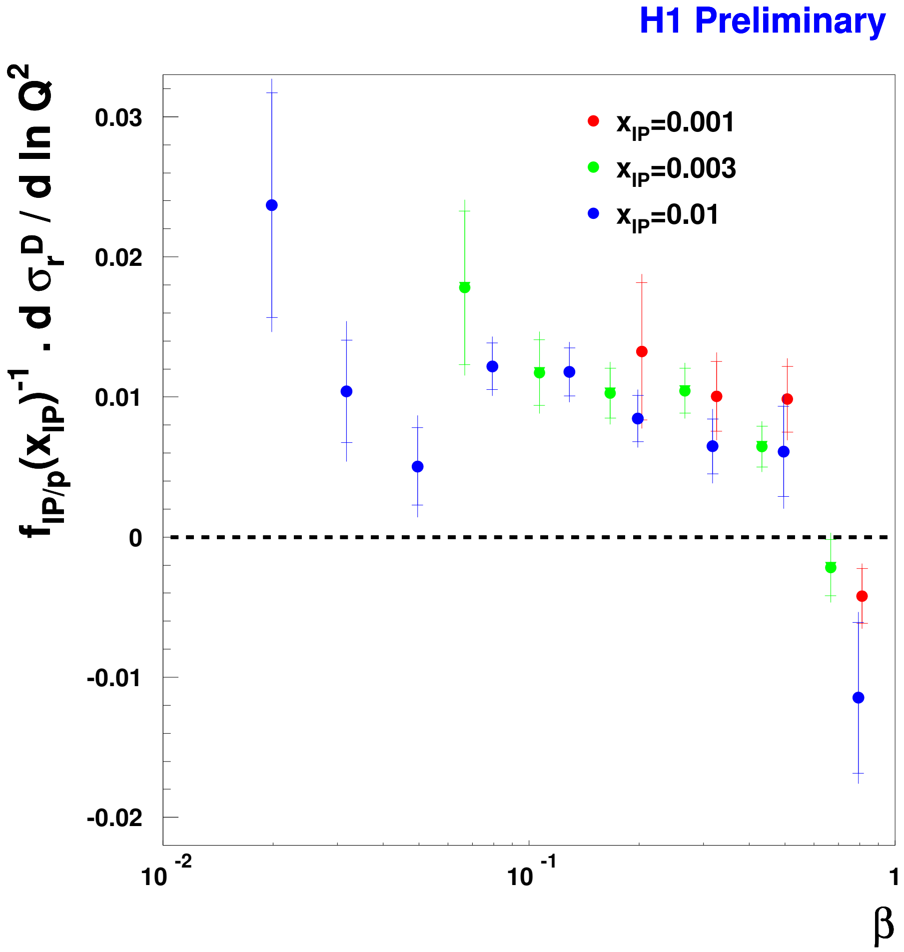

Figure 6: Logarithmic Q^2 derivatives of σ_r^D for different β and $x_{I\!P} = 0.001, 0.003, 0.01$, scaled at each $x_{I\!P}$ by the values assumed for the t-integrated pomeron flux in the QCD fits (equation 14).

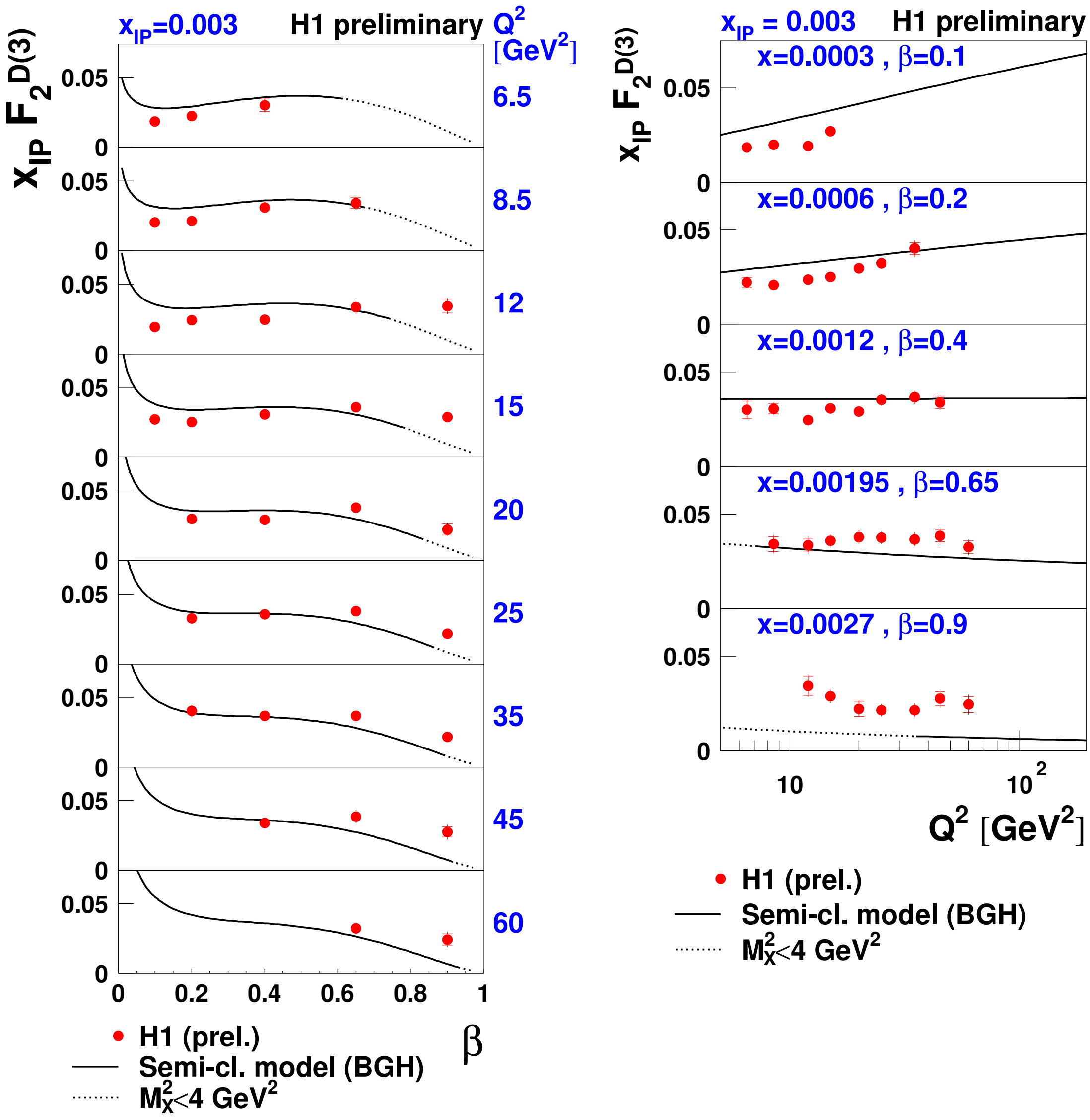

Figure 7: The diffractive structure function $x_{\mathbb{P}} F_2^{D(3)}(\beta, Q^2, x_{\mathbb{P}})$, extracted from the measured reduced cross section $\sigma_r^{D(3)}$ under the assumption of $F_L^D = 0$, at fixed $x_{\mathbb{P}} = 0.003$, plotted as a function of β for various values of Q^2 *(left)* and as a function of Q^2 for various values of β *(right)*. The data are compared with the predictions of the semi-classical model by Buchmüller, Gehrmann and Hebecker [32] *(solid curves)*. The dotted curves correspond to an extension of the model into the region of small $M_X < 2$ GeV, where the model is not expected to be valid.

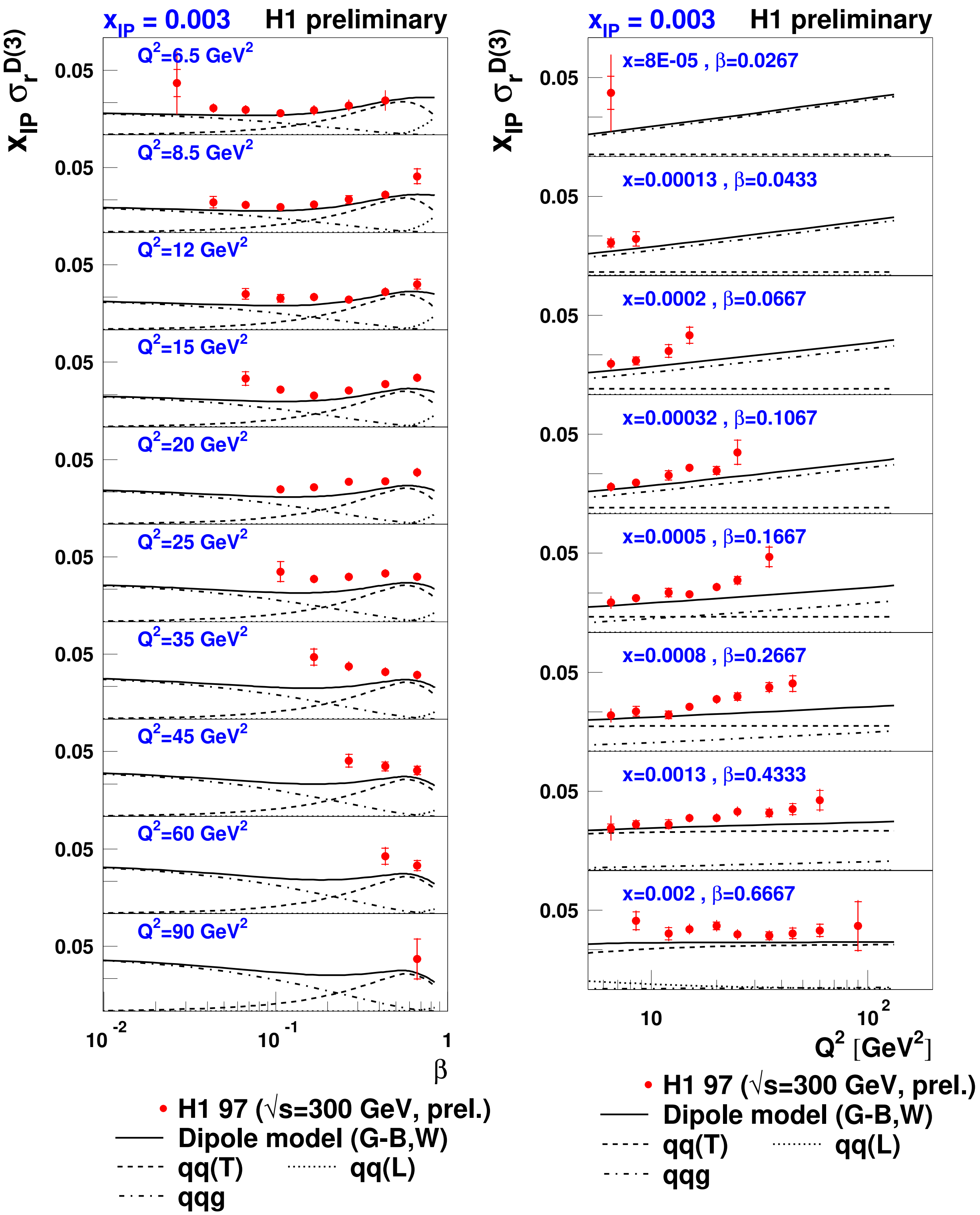

Figure 8: The diffractive reduced cross section $\sigma_r^{D(3)}$ at fixed $x_{I\!P} = 0.003$, plotted as a function of β for various values of Q^2 *(left)* and as a function of Q^2 for various values of β *(right)*. The data are compared with the prediction of a colour dipole model by Golec-Biernat and Wüsthoff [33, 34] *(solid curves)*. The contributions in the model from $\gamma^* \to q\bar{q}_T$ (*dashed*), $\gamma^* \to q\bar{q}_L$ (*dotted*) and $\gamma^* \to q\bar{q}g_T$ (*dash-dotted*) virtual photon fluctuations are shown separately.

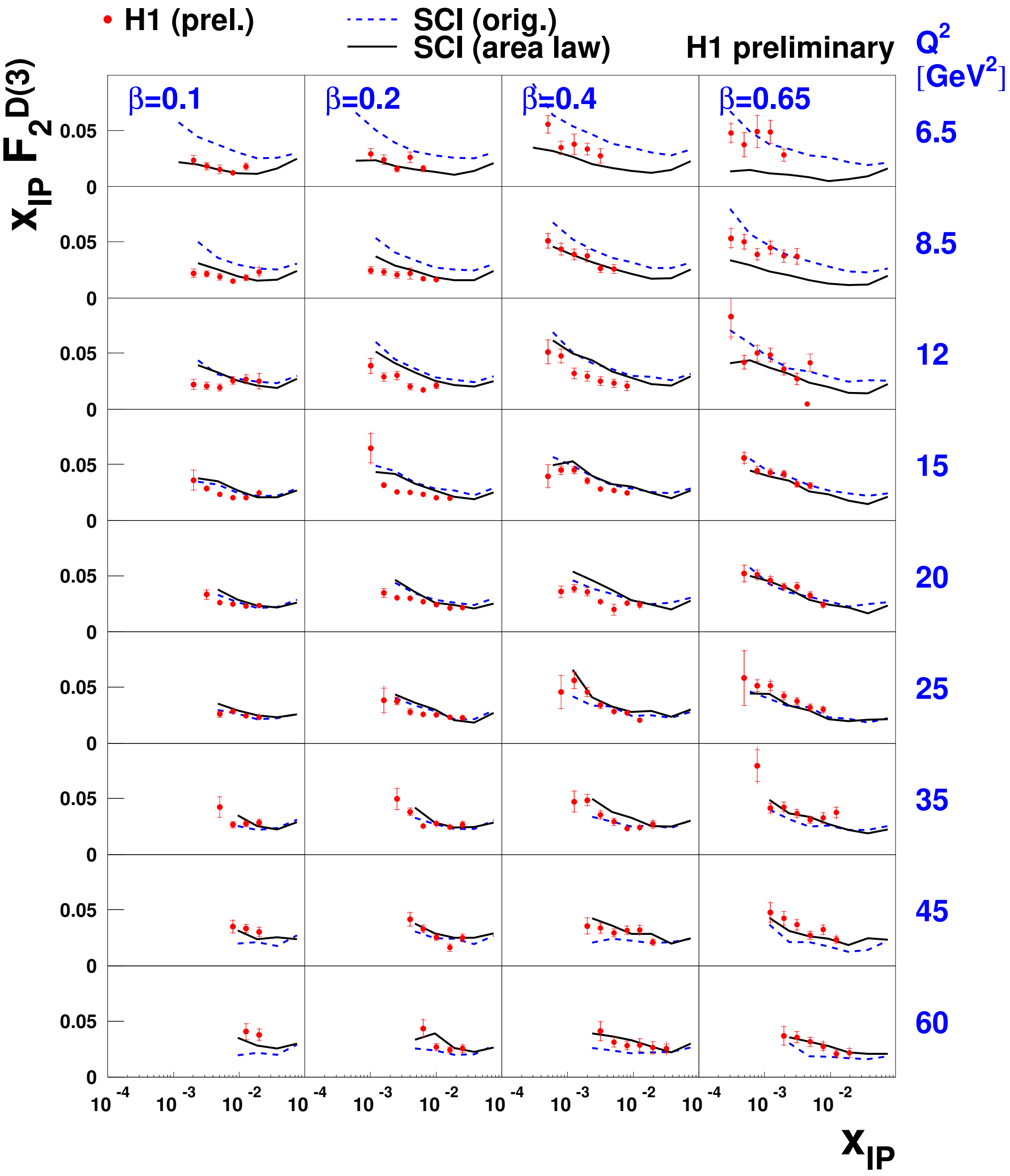

Figure 9: The diffractive structure function $x_{I\!P} F_2^{D(3)}(\beta, Q^2, x_{I\!P})$, extracted from the measured reduced cross section $\sigma_r^{D(3)}$ under the assumption of $F_L^D = 0$, plotted as a function of $x_{I\!P}$ at fixed values of Q^2 and β. Only a sub-sample of the data, corresponding to $0.1 \leq \beta \leq 0.65$ and $Q^2 \leq 60\ \mathrm{GeV}^2$, are shown. The data are compared with the predictions of the original Soft Colour Interactions (SCI) model [35] *(dashed curves)* and its refinement based on a generalised area law [36] *(solid curves)*. The predictions have been obtained using the LEPTO $6.5.2\beta$ Monte Carlo generator [37].

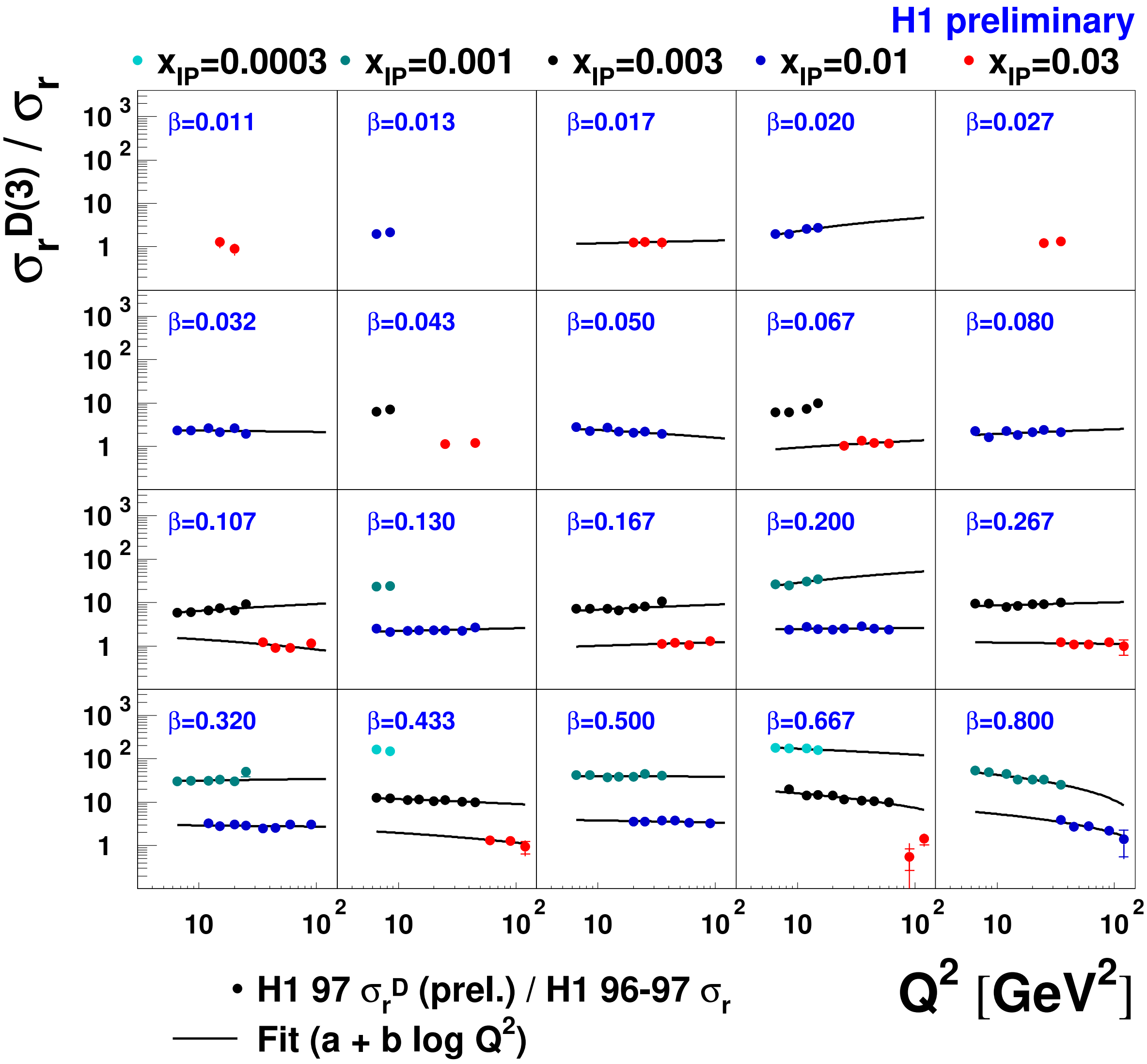

Figure 10: The ratio of diffractive to inclusive reduced cross sections, shown as a function of Q^2. The results of the fit to a logarithmic Q^2 dependence are overlaid (figure 11). The Q^2 dependence of the ratio is small for most β and varies little with $x_{I\!P}$.

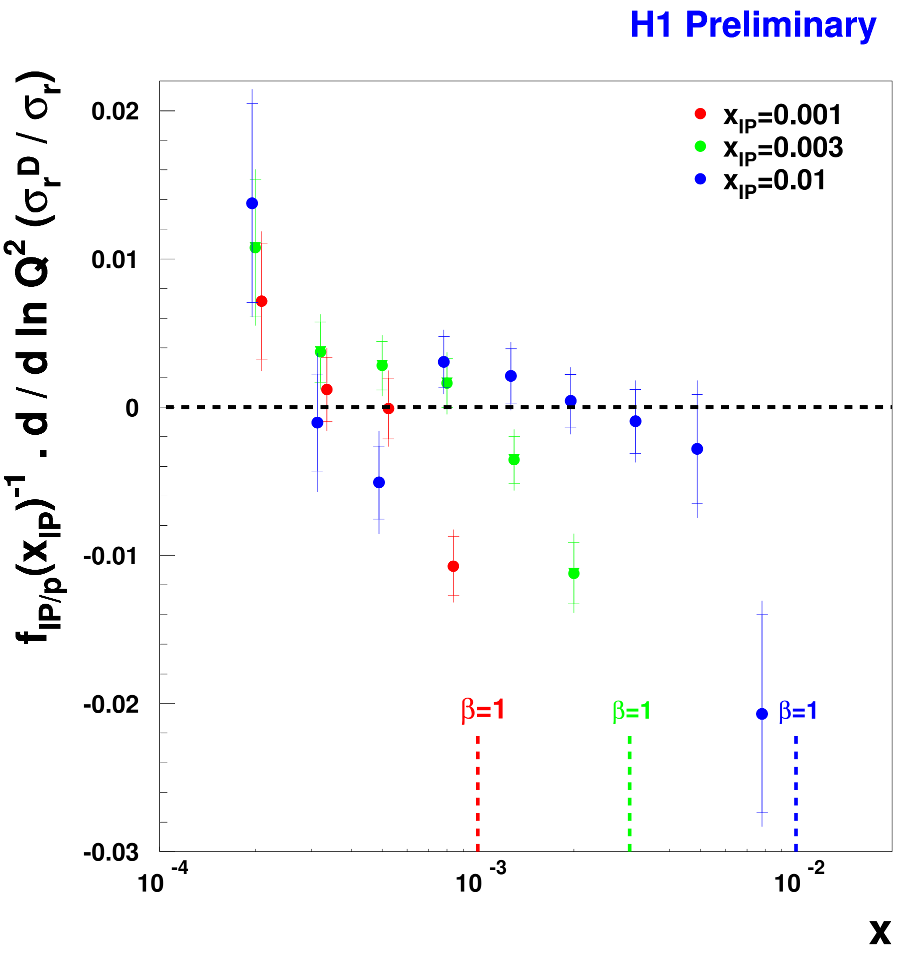

Figure 11: Logarithmic Q^2 derivatives of the ratio σ_r^D/σ_r, the $x_{I\!P}$ dependence of σ_r^D having been divided out using a parameterisation of the $x_{I\!P}$ dependence (equation 14). The data are consistent with identical Q^2 dependences of the diffractive and inclusive cross sections away from $\beta = 1$, with clear differences from this behaviour as $\beta \to 1$.

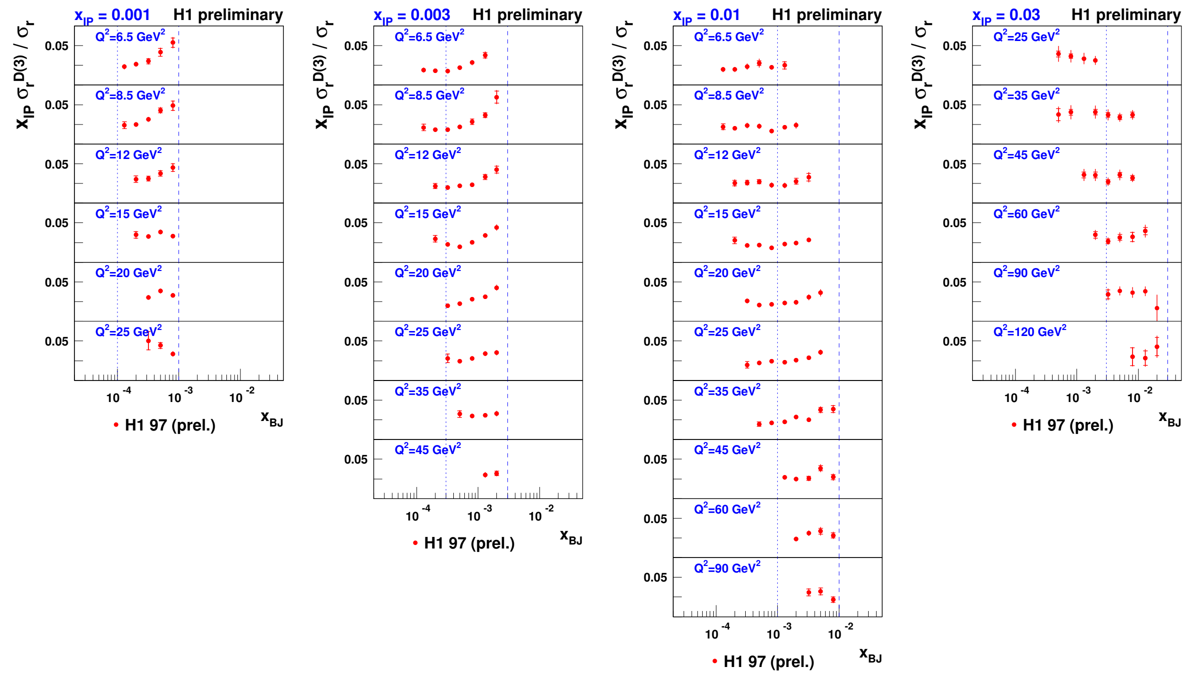

Figure 12: The ratio of diffractive to inclusive reduced cross sections, shown as a function of x at fixed $x_{\mathbb{P}}$ and Q^2 values. Note that $M_{\rm X}^2 = Q^2(x_{\mathbb{P}}/x - 1)$ varies with x in these plots. The dashed (dotted) lines indicate the points at which $\beta = 1$ ($\beta = 0.1$). Clear variations in the shape are observed for the different $x_{\mathbb{P}}$ values, arising from the fact that they cover different β ranges. For the high β region, the ratio has a complicated shape, since σ_r^D has considerable structure in this region, whereas σ_r is well parameterised by $x^{-\lambda}$. For the lowest β, a flatter dependence of the ratio on x is observed.

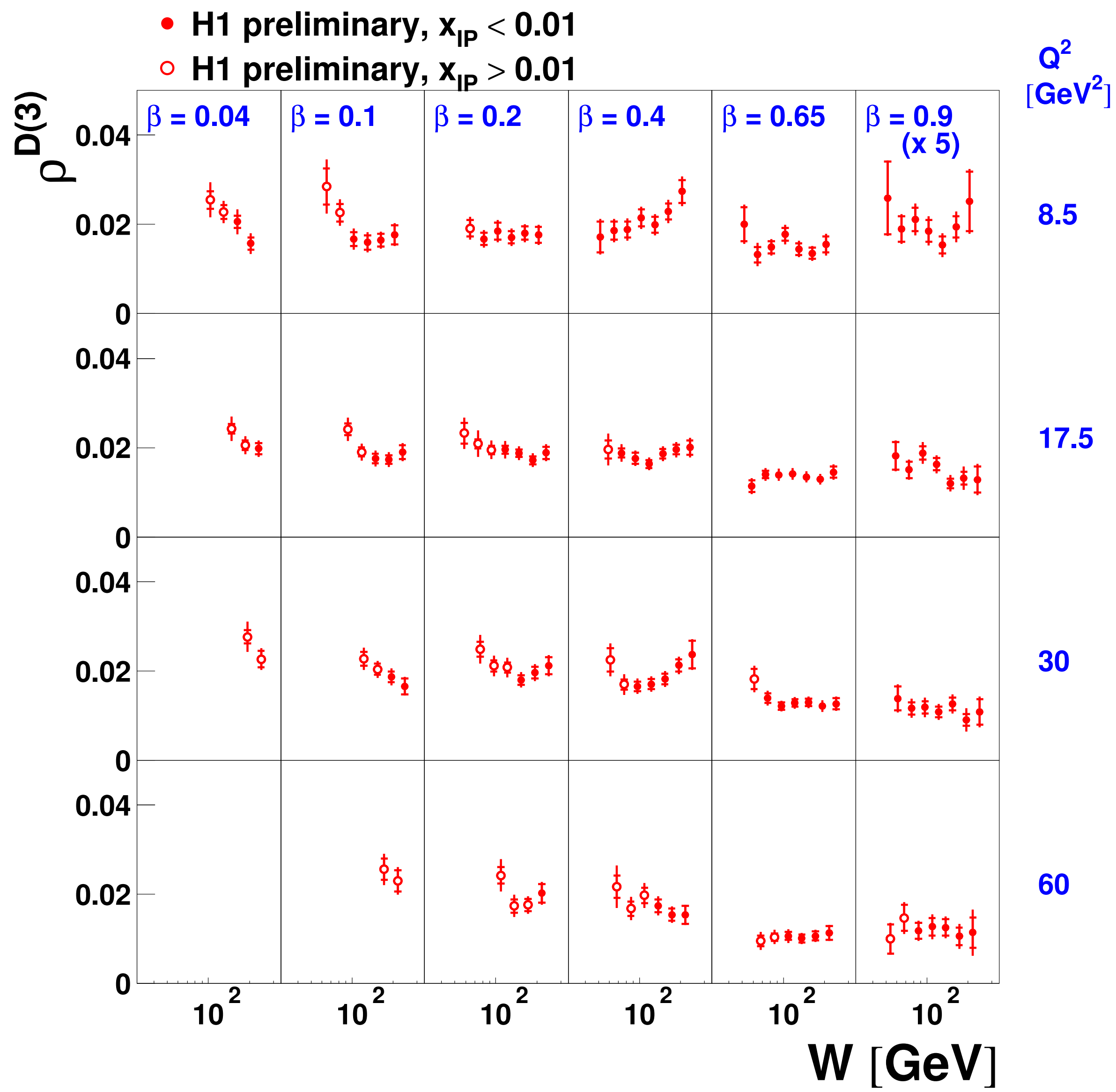

Figure 13: Measurements of $\rho^{D(3)}$, illustrating the ratio of the diffractive to the inclusive cross section. The data points at $\beta = 0.9$ have been scaled by a factor of 5 for visibility. The filled points correspond to the region $x_{I\!P} < 0.01$ in the diffractive measurement. The open points correspond to $x_{I\!P} > 0.01$. At each β and Q^2 point, the photon dissociation mass is fixed according to $M_{\rm x}^2 = Q^2\ (1/\beta - 1)$.

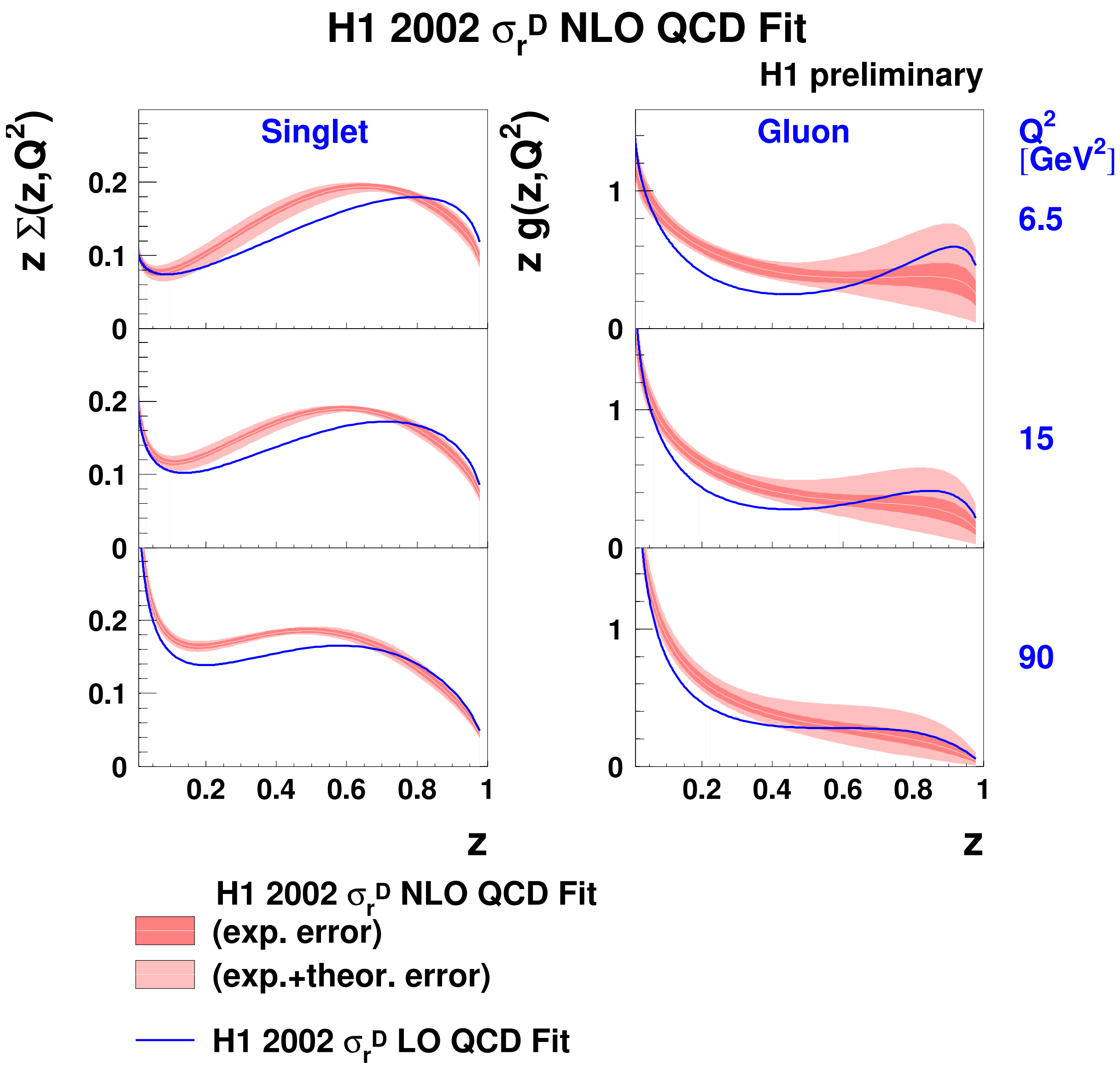

Figure 14: Diffractive parton densities obtained from the QCD fit, normalised such that the 'pomeron flux' is unity at $x_{I\!P} = 0.003$. The left hand side shows the singlet quark distribution ($6 * u$ where we assume $u = d = s = \bar{u} = \bar{d} = \bar{s}$). The right hand side shows the gluon density. The red bands show the results of the NLO fits, with inner error bands showing the experimental errors (statistical and systematic) and the outer errors bands showing the full uncertainties, including those arising from theoretical assumptions. For comparison, the central values of the parton densities extracted from the LO fit are also shown (blue line).

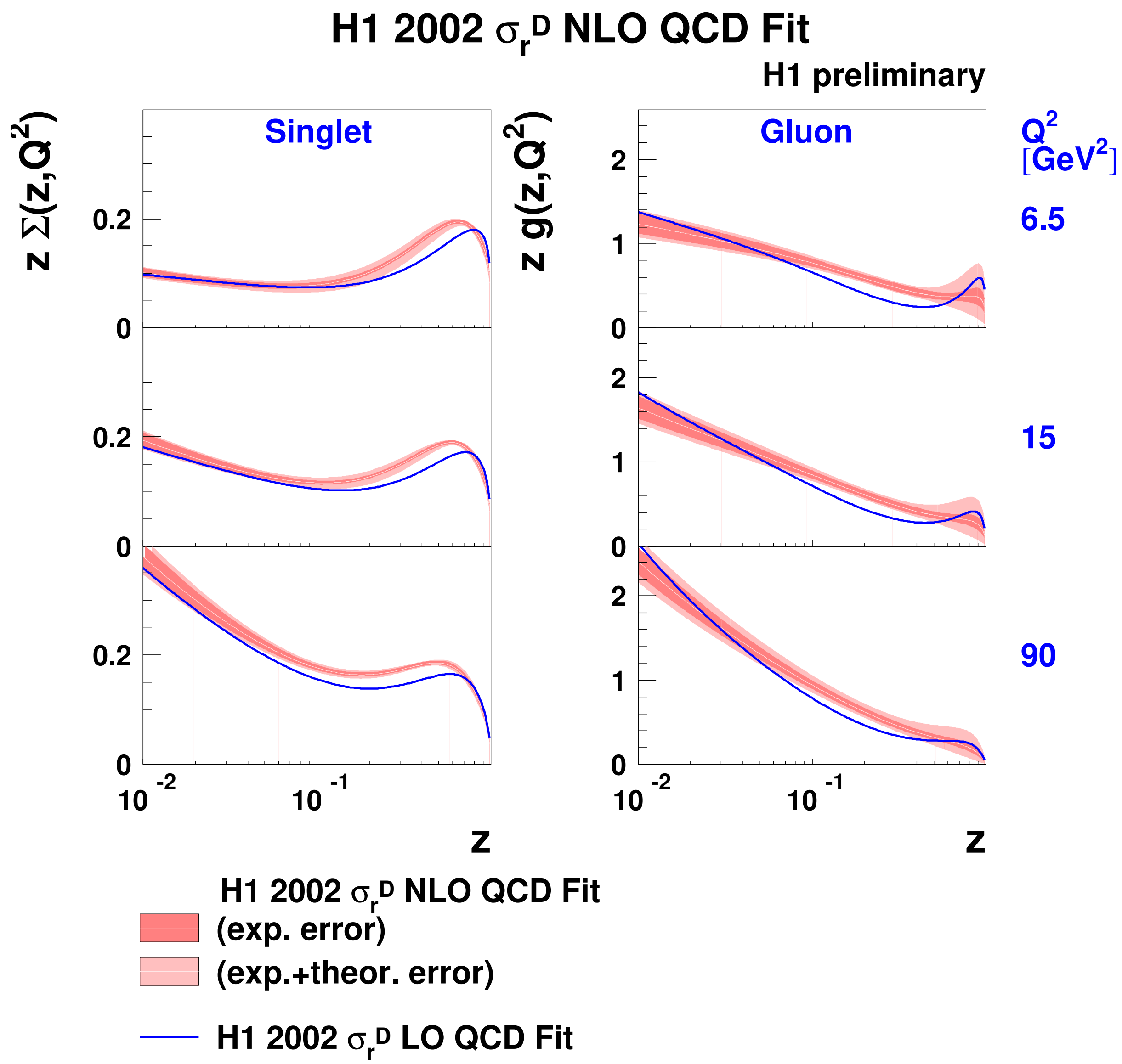

Figure 15: The same plot as figure 14, but on a logarithmic z scale.

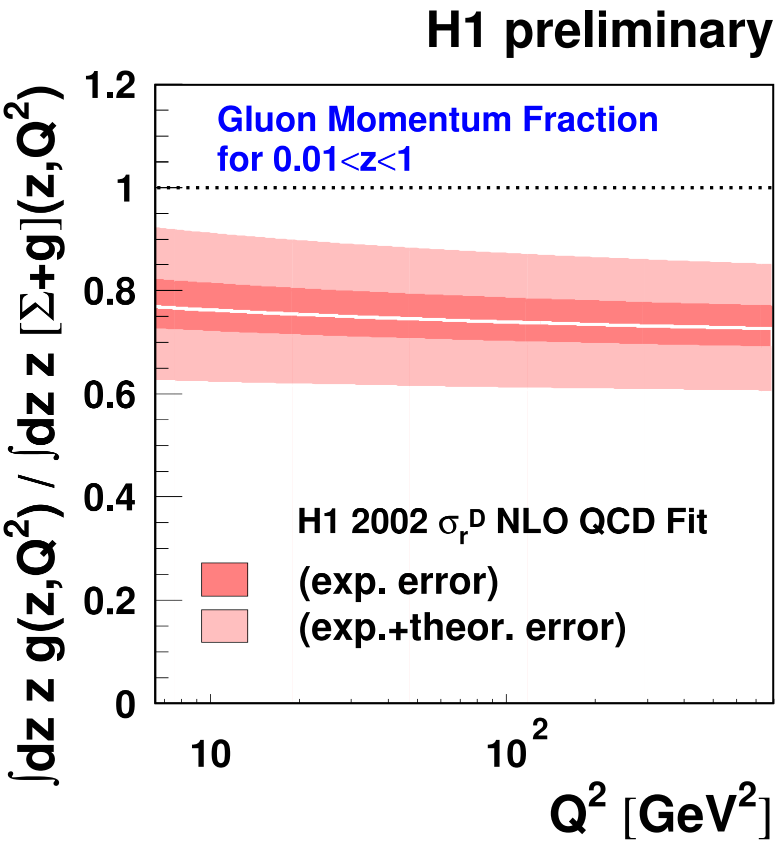

Figure 16: The fraction of the overall diffractive exchange momentum carried by gluons in the NLO fits, integrated over the z range measured and shown as a function of Q^2. The error bands again reflect the experimental (inner) and combined experimental and theoretical (outer) uncertainties.

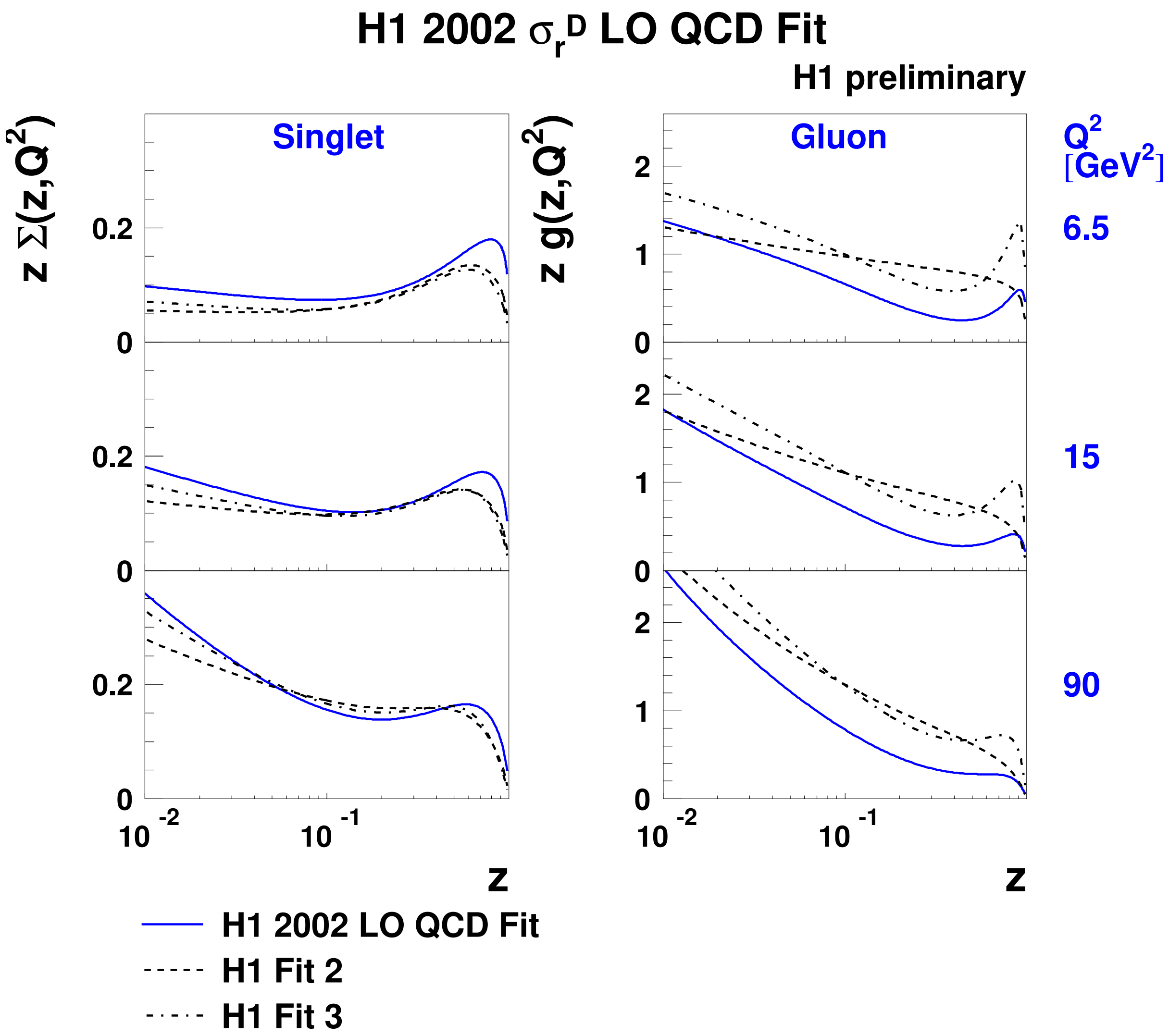

Figure 17: Comparison of the central values of the parton densities from the LO fit compared with the results of the two fits including glouns at the starting scale made to the 1994 H1 data [3]. The agreement in the singlet quark density is reasonable for $z < 0.65$ as used in the fits. The shape of the gluon is fairly similar to 1994 fit 3 ('peaked' gluon), except that the peak at highest z is significantly smaller. The normalisation of the gluon is different by about 30% for low-medium z, a difference which would be inside the combined errors on the two extractions.

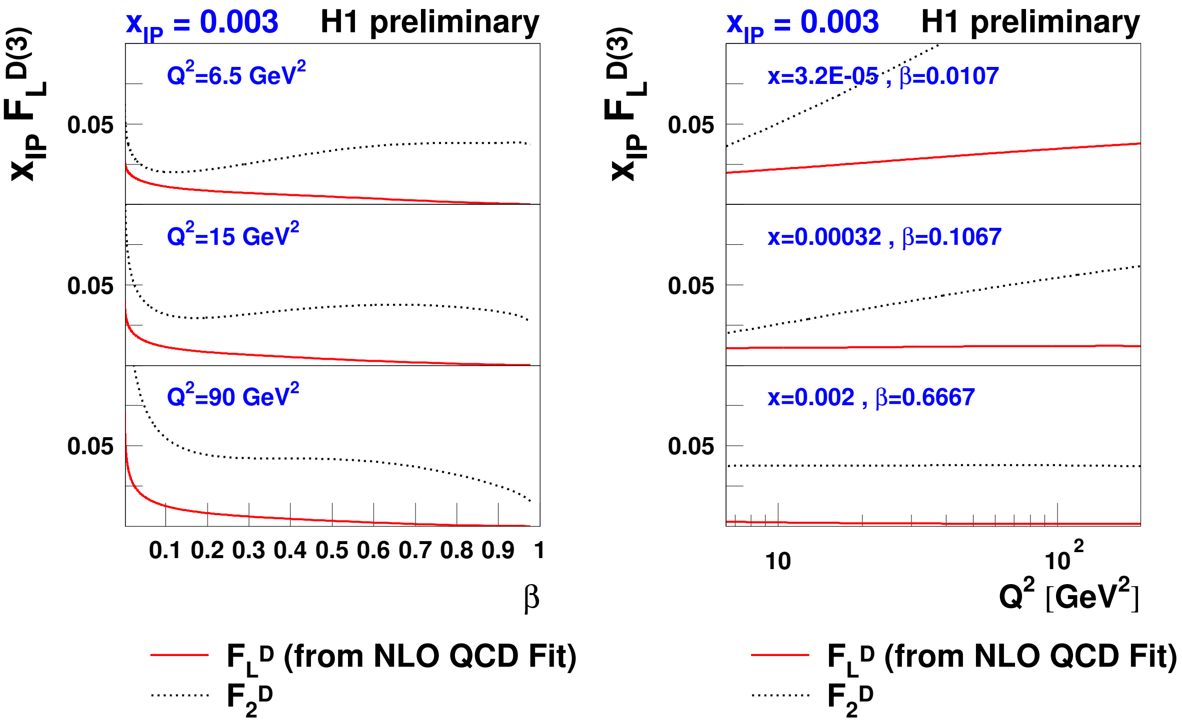

Figure 18: The leading twist component of F_L^D as obtained from the NLO QCD fit compared with its maximum possible value of F_2^D. The values of F_L^D are comparatively large, since they are closely related to the (dominant) gluon density at NLO.

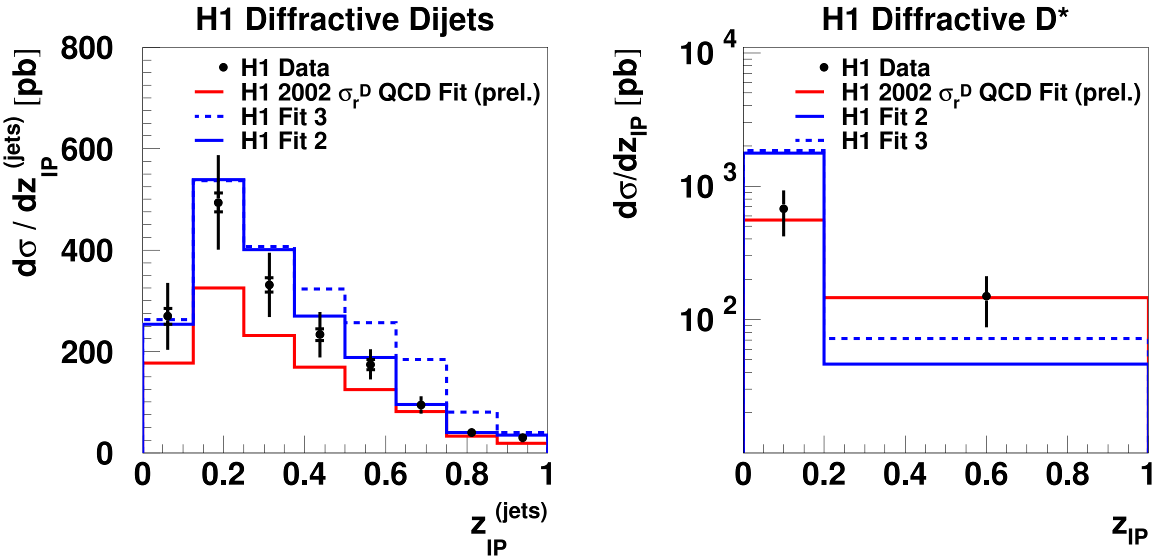

Figure 19: H1 measurements of diffractive DIS dijet ([11], *left*) and D^* meson ([12], *right*) hadron level cross sections, differential in $z_{I\!P}$, compared with the present LO QCD fit as described in section 5 as well as the fits to the previous data from [3] ('H1 fit 2' and 'H1 fit 3'). The comparisons are obtained using the RAPGAP program and for the scale set to $\mu^2 = Q^2 + p_T^2 + m_q^2$.

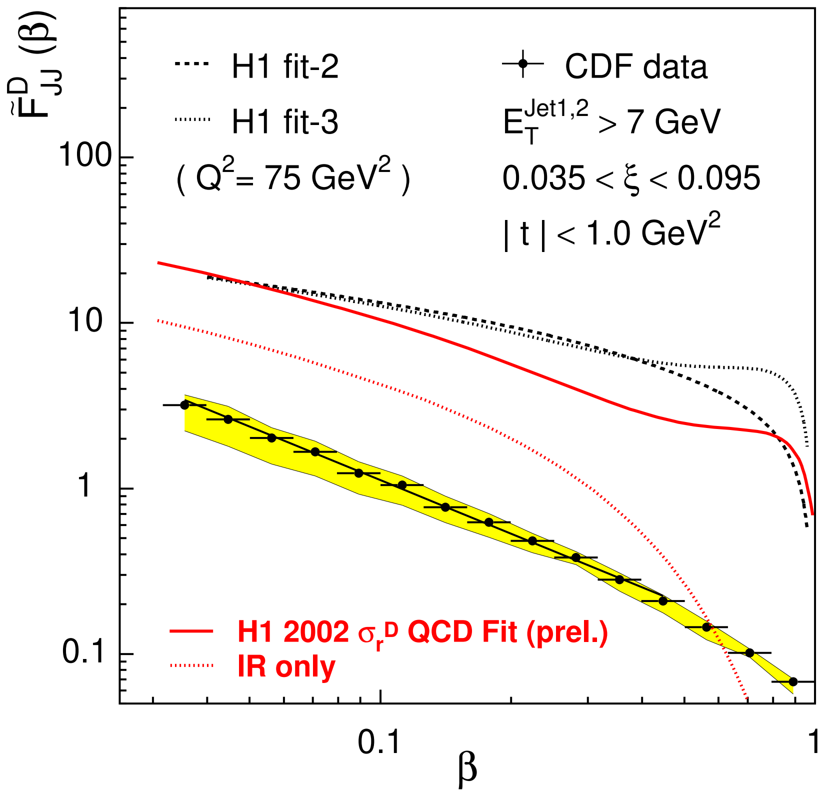

Figure 20: The quantity $\tilde{F}^D_{JJ}(\beta)$ as extracted from diffractive dijet data by the CDF collaboration [13], compared with the predictions of the new and old ([3]) LO QCD fits. Assuming Regge and QCD hard scattering factorisation, $\tilde{F}^D_{JJ}(\beta)$ corresponds to a convolution of the diffractive (and sub-leading) exchange parton densities with the appropriate flux factors. The new fits are slightly closer to the data at large β, but a large discrepancy of approximately one order of magnitude remains. In contrast to the comparison with the fits to 1994 data, the rapidity gap survival probability appears to be approximately constant over most of the β range. The predicted contribution of sub-leading exchanges is approximately 50% at low β, somewhat smaller than that from the old QCD fits.

A Additional Figures

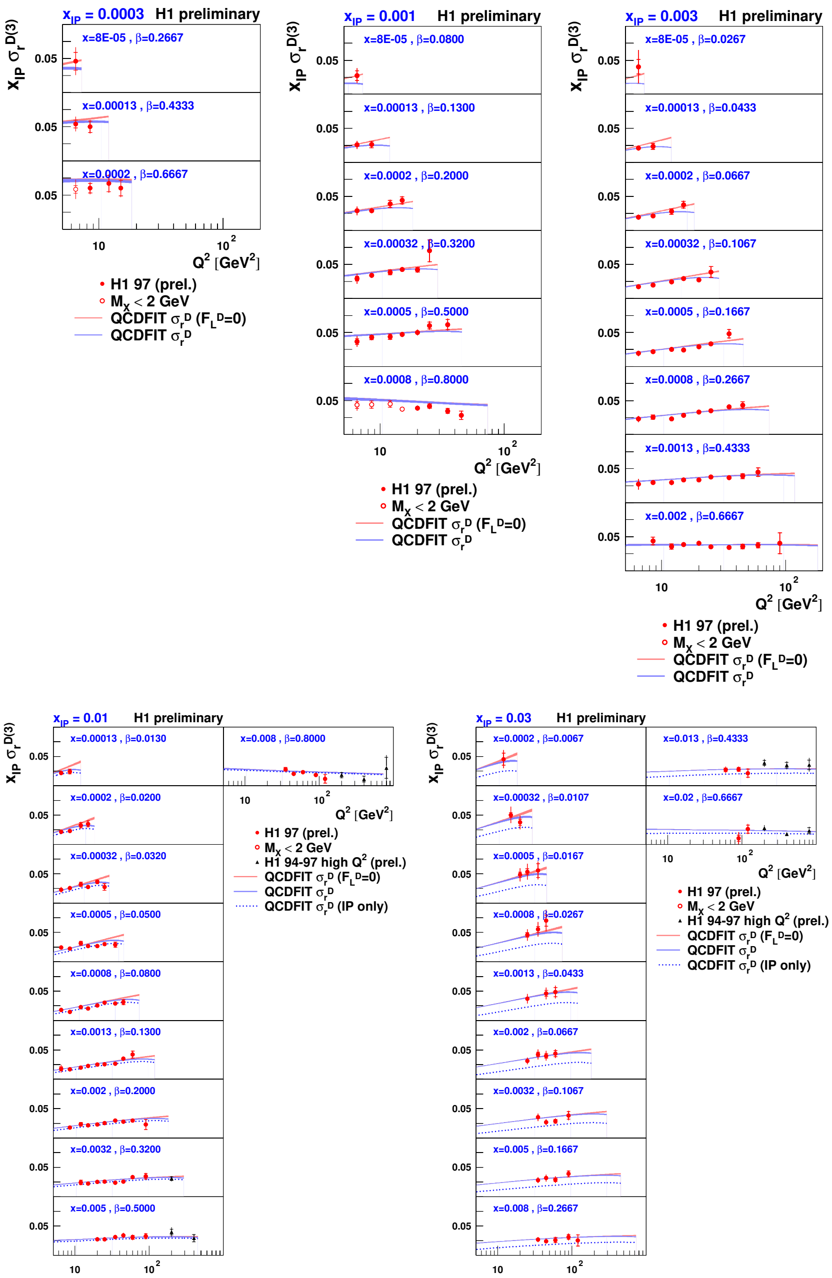

Figure A1: Reduced diffractive cross section data for fixed $x_{I\!P} = 0.0003, 0.001, 0.003, 0.01, 0.03$ and fixed x or β, shown as a function of Q^2 and compared with the results of the NLO QCD fit (experimental errors only). The filled data points were included in the fit. The open data points ($M_{\rm X} < 2$ GeV) were omitted. In addition to the present measurement, H1 preliminary data at higher Q^2 [5] are shown. The predictions of the NLO fit for F_2^D (i.e. σ_r^D for $F_L^D = 0$) are also shown, as well as the contribution to the predicted reduced cross section from the leading diffractive exchange alone (the remainder being assigned to sub-leading meson exchange).

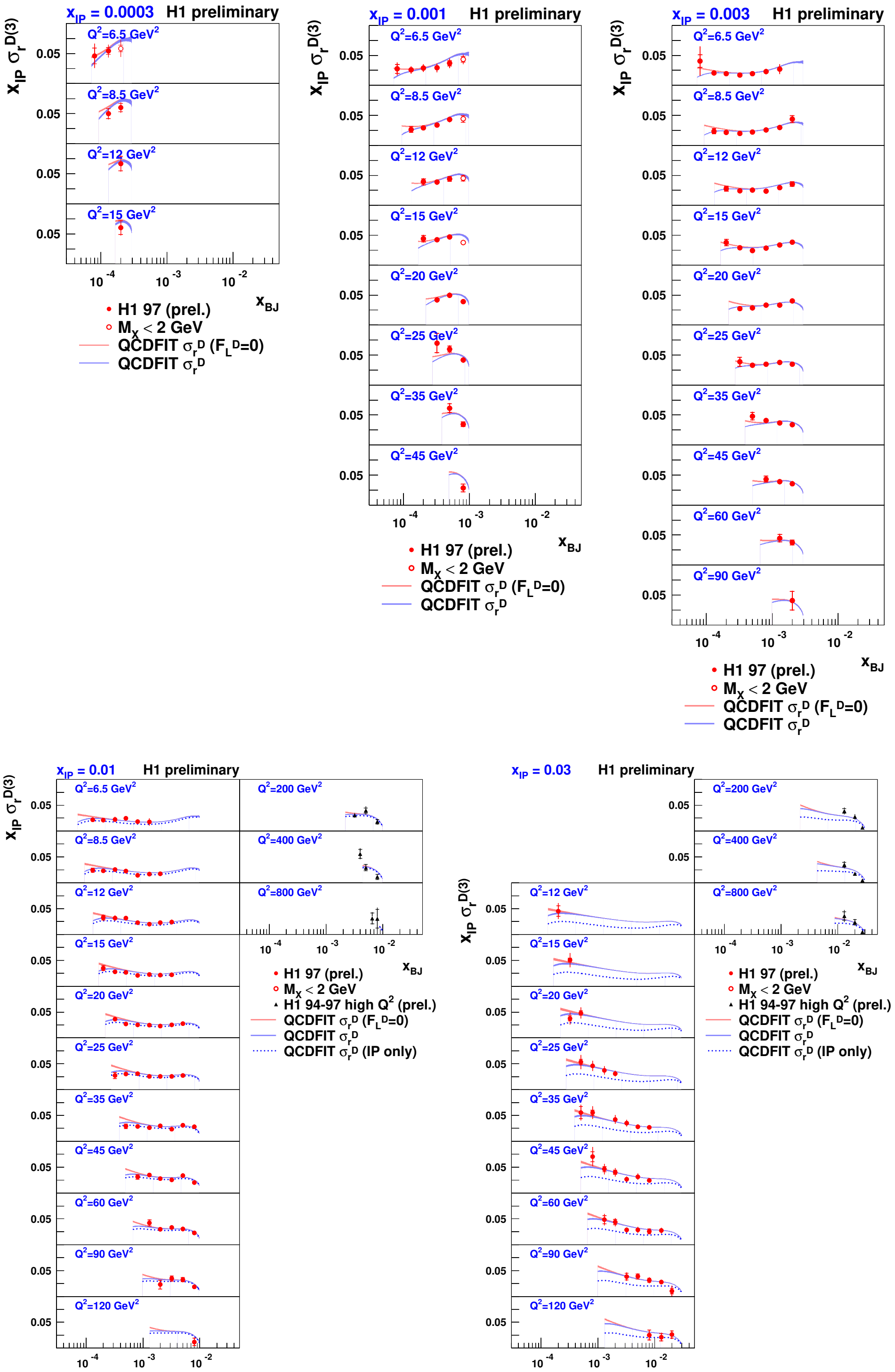

Figure A2: Reduced diffractive cross section data for fixed $x_{I\!P} = 0.0003, 0.001, 0.003, 0.01, 0.03$ and fixed Q^2, shown as a function of x and compared with the results of the NLO QCD fit. The shape of the distributions at fixed Q^2 varies with $x_{I\!P}$, since different regions of β are probed for the different $x_{I\!P}$ values. Note that the cross section is constrained to tend to zero as $x \to x_{I\!P}$ ($\beta \to 1$).

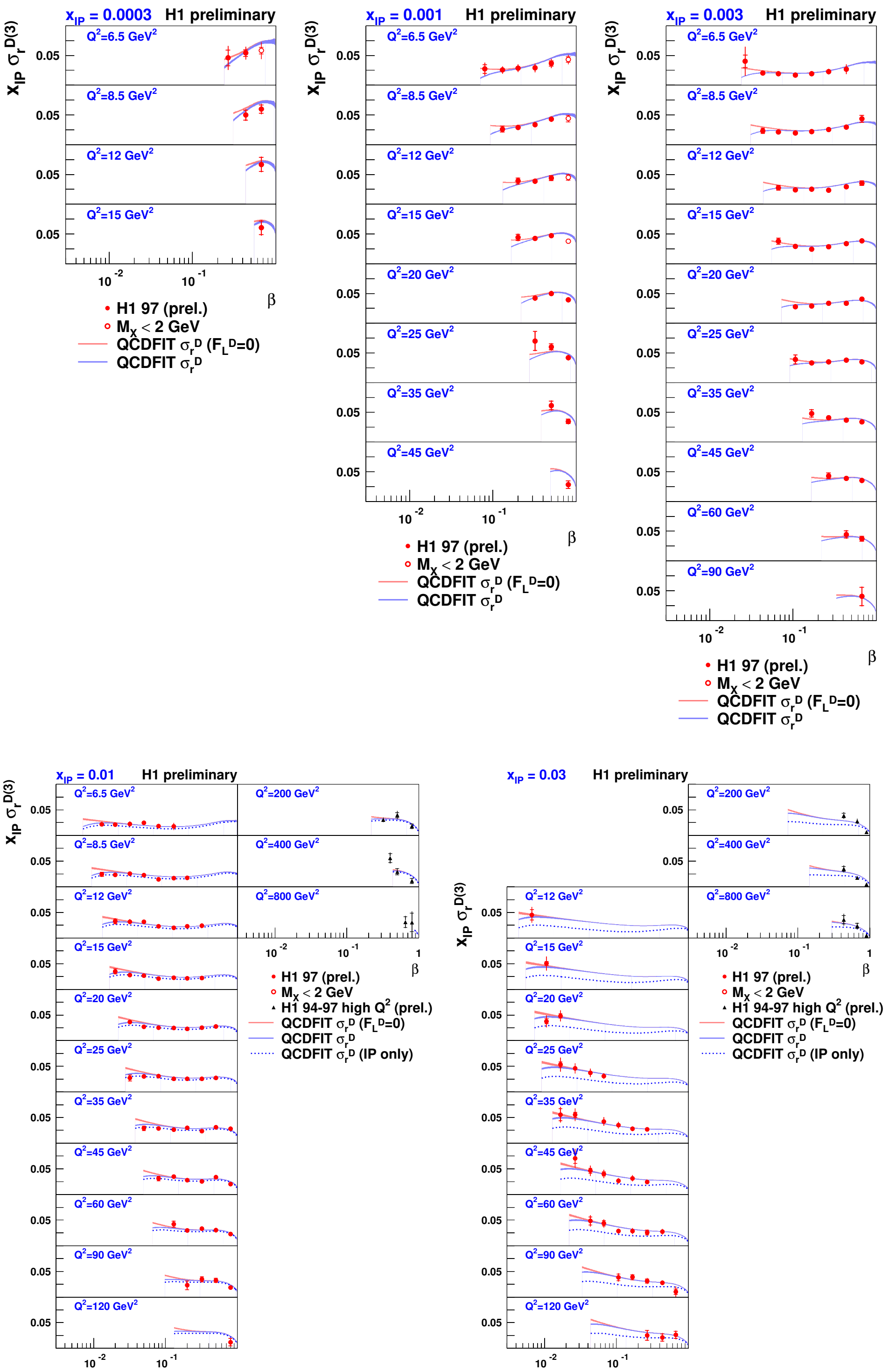

Figure A3: Reduced diffractive cross section data for fixed $x_{I\!P}$ = $0.0003, 0.001, 0.003, 0.01, 0.03$ and fixed Q^2, shown as a function of β and compared with the results of the NLO QCD fit. The shape of the distributions at fixed Q^2 is similar for different $x_{I\!P}$ values.

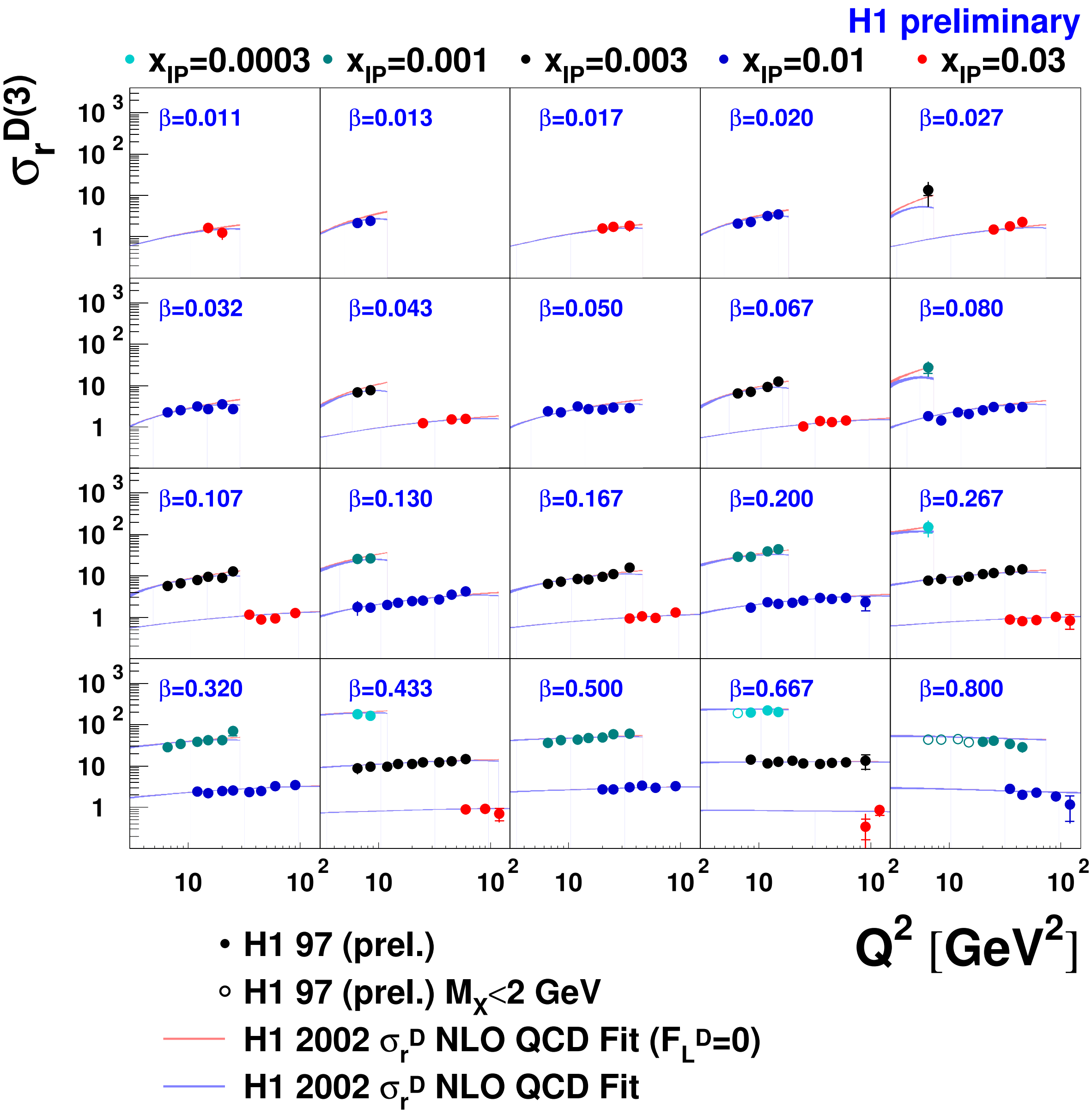

Figure A4: Q^2 dependence of the reduced cross section at fixed $x_{I\!P} = 0.0003, 0.001, 0.003, 0.01, 0.03$ and fixed β or x, compared with the predictions of the NLO QCD fit. The filled data points were included in the fit. The open data points ($M_x < 2$ GeV) were omitted. The predictions of the NLO fit for F_2^D (i.e. σ_r^D for $F_L^D = 0$) are also shown.

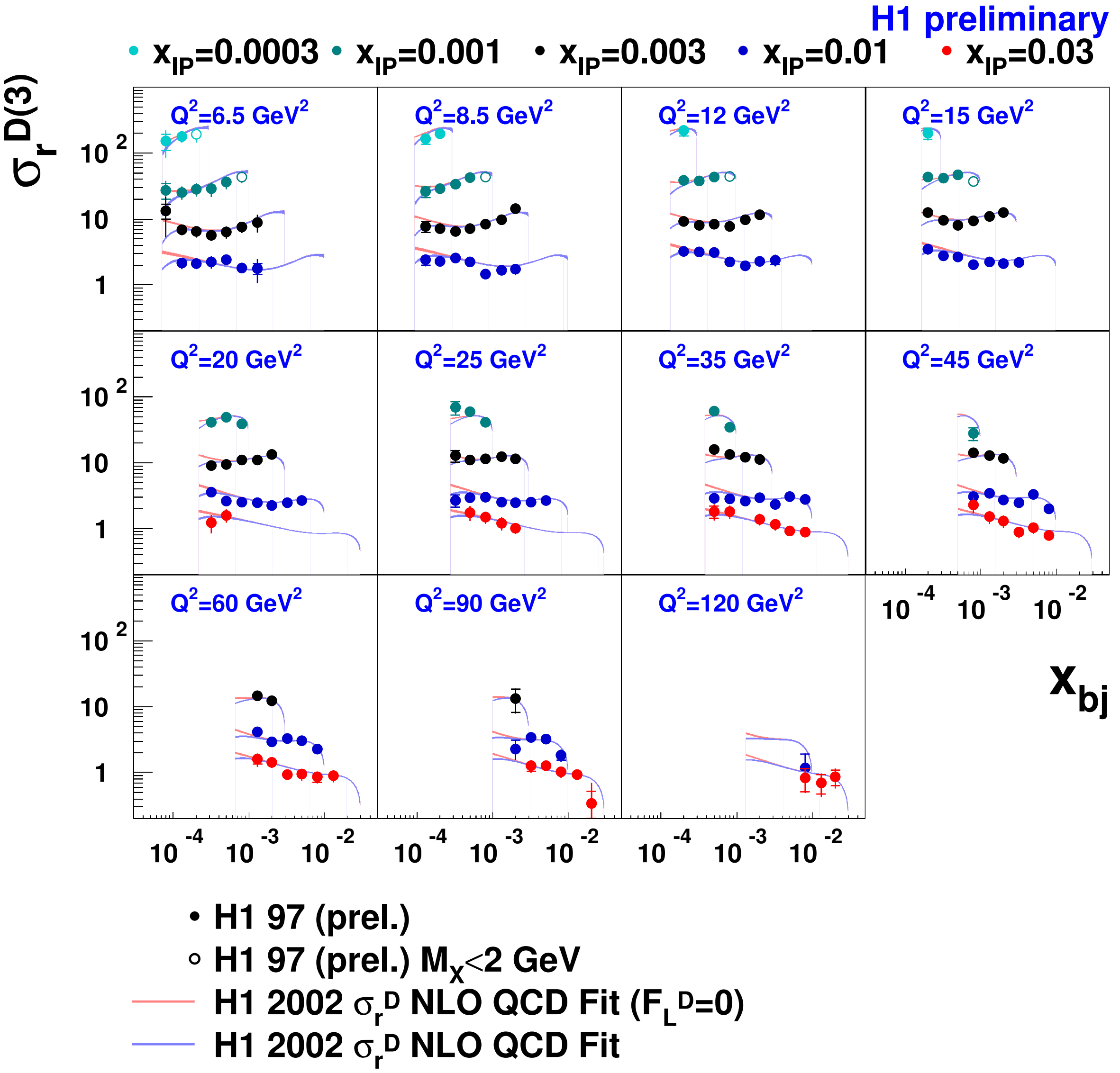

Figure A5: x dependence of the reduced cross section at fixed $x_{I\!P} = 0.0003, 0.001, 0.003, 0.01, 0.03$ and fixed Q^2, compared with the predictions of the NLO QCD fit.

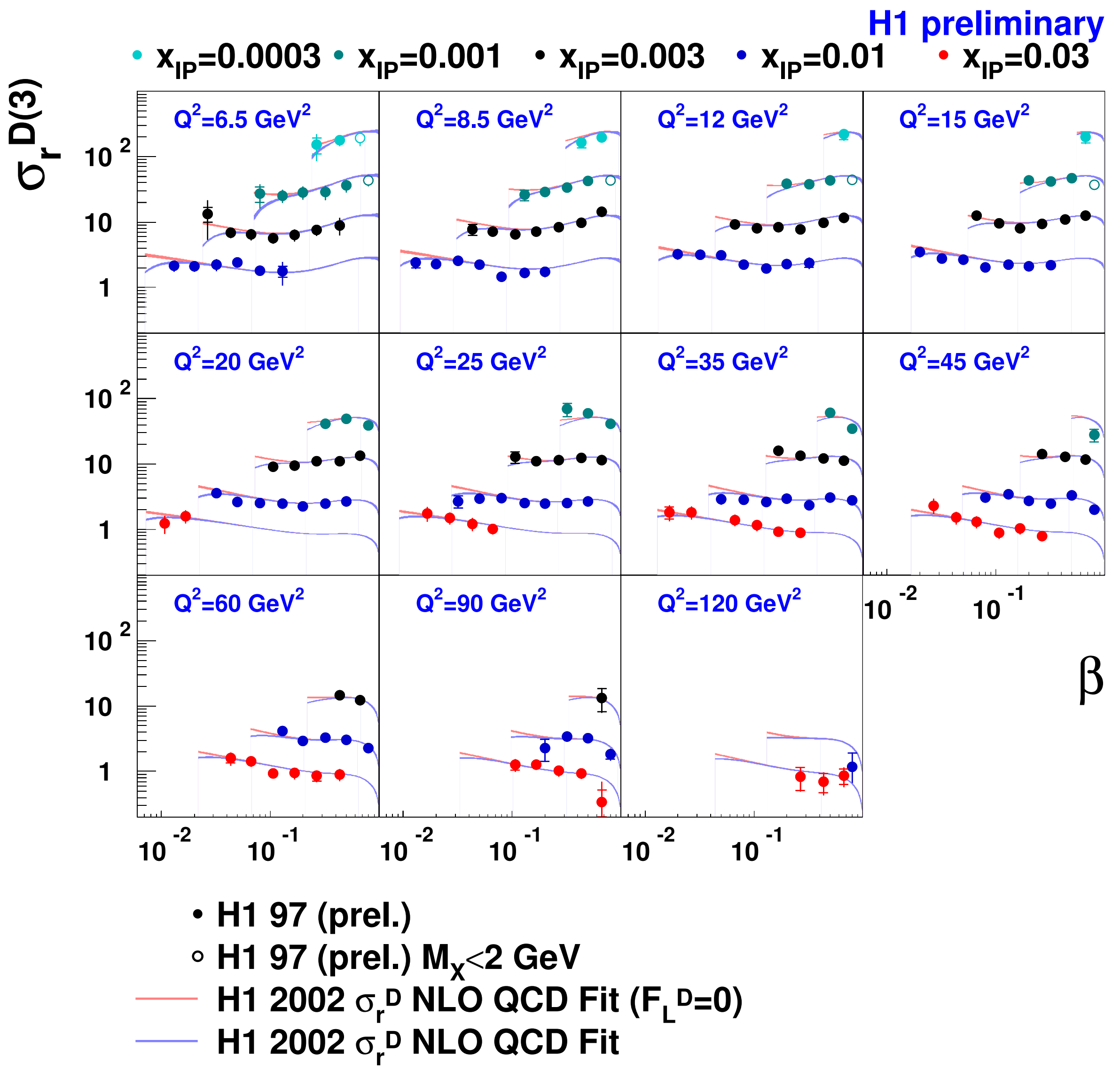

Figure A6: β dependence of the reduced cross section at fixed $x_{I\!P} = 0.0003, 0.001, 0.003, 0.01, 0.03$ and fixed Q^2, compared with the predictions of the NLO QCD fit.

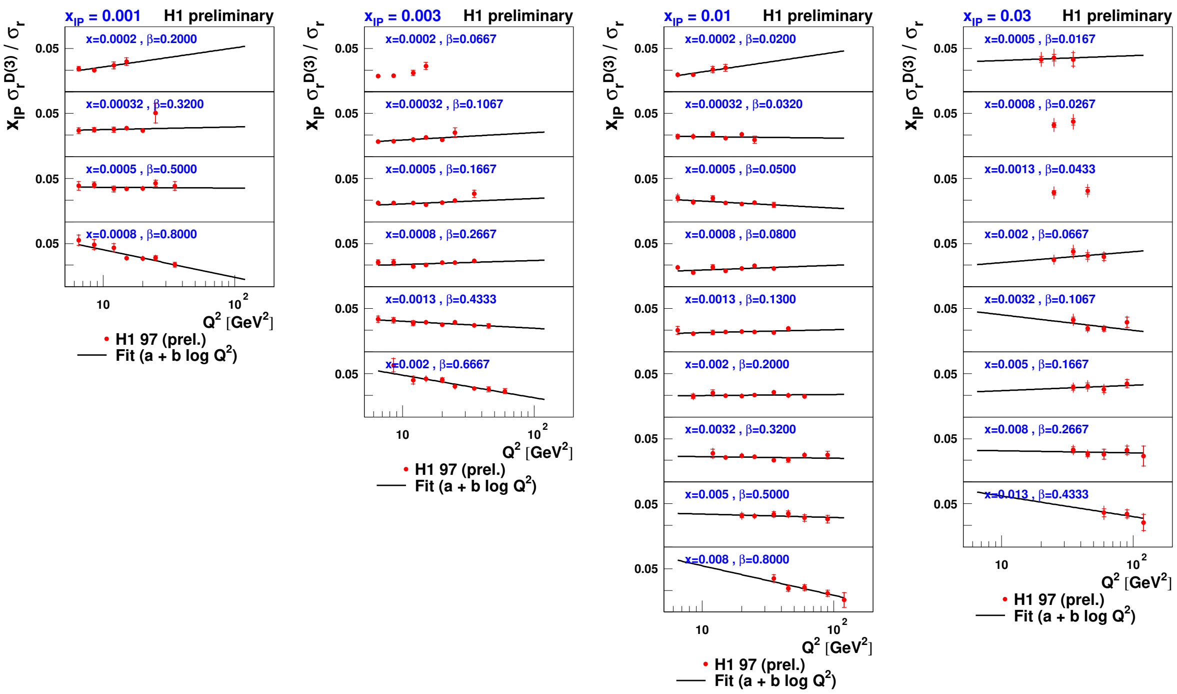

Figure A7: The ratio of diffractive to the inclusive reduced cross section, shown as a function of Q^2 in different $x_{I\!P}$ and x bins. The results of the fit to a logarithmic Q^2 dependence are overlaid (figure 11). The Q^2 dependence of the ratio is small except at the highest β and varies little with $x_{I\!P}$.

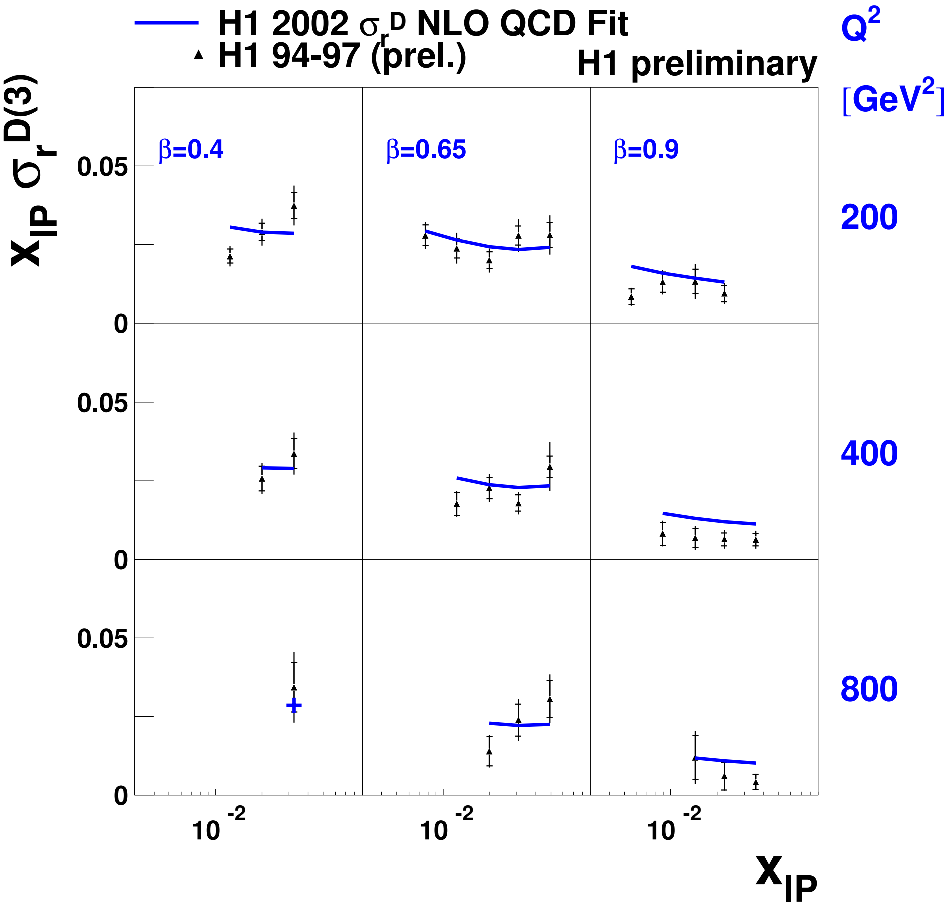

Figure A8: High Q^2 data on the diffractive reduced cross section $\sigma_r^{D(3)}$ [5] compared with the predictions of the NLO QCD fit. The data were included in the fit.

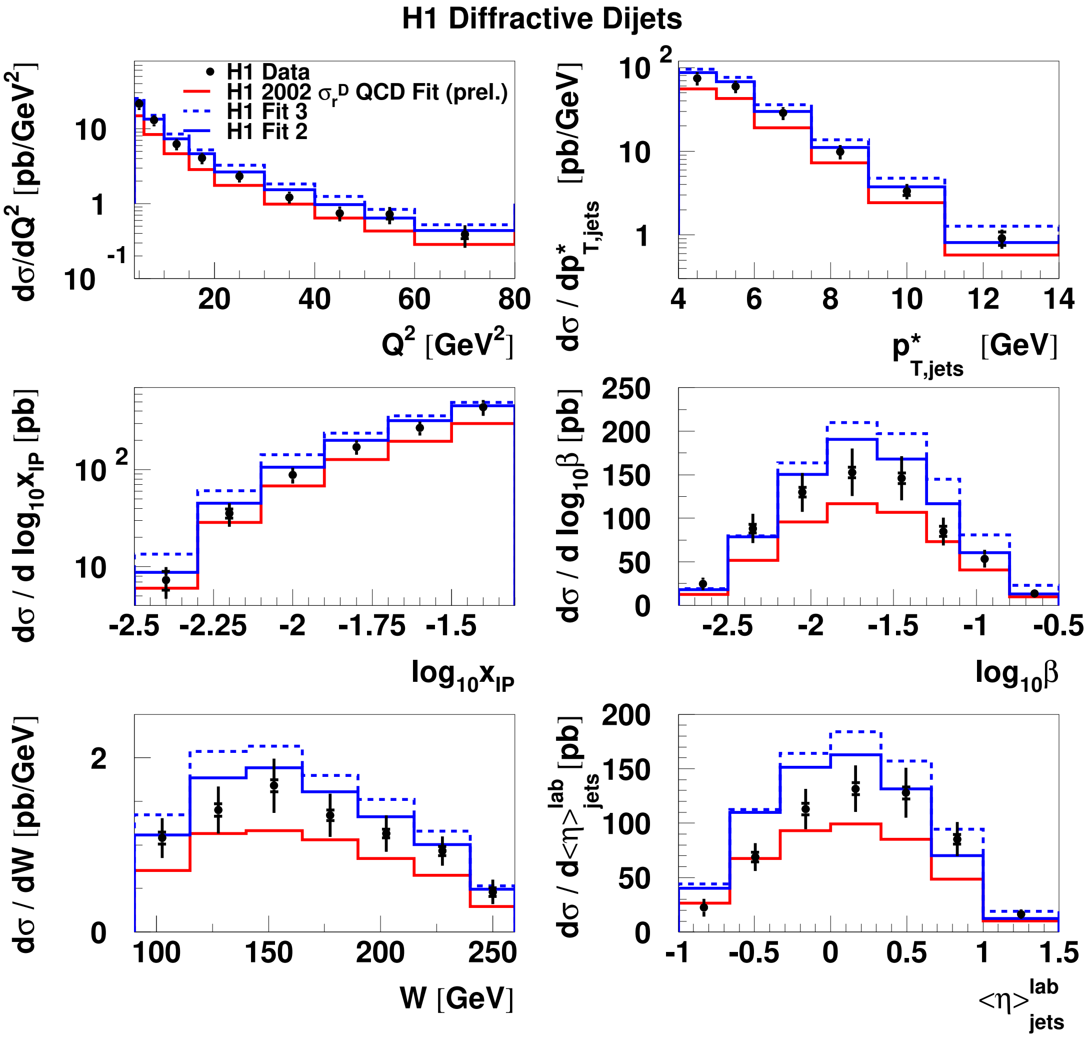

Figure A9: H1 measurements of diffractive dijets [11] compared with the new and old [3] LO QCD fits. The dijet cross sections differential in Q^2, the jet transverse momentum in the $\gamma^* p$ centre of mass frame $p^*_{\mathrm{T,jets}}$, $\log_{10} x_{I\!P}$, $\log_{10}\beta$, W and the mean dijet pseudorapidity in the laboratory frame $\langle\eta\rangle^{\mathrm{lab}}_{\mathrm{jets}}$ are shown.

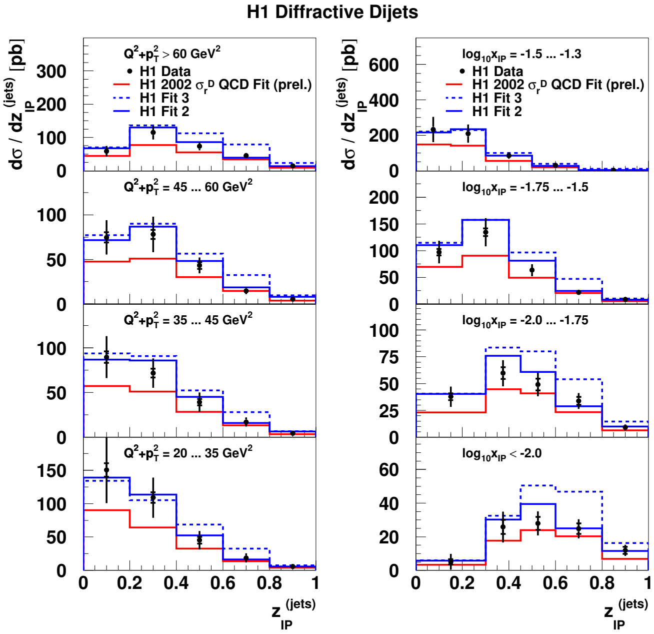

Figure A10: H1 measurements [11] of diffractive dijet cross sections as a function of $z_{I\!P}^{\rm jets}$ in different intervals of $Q^2 + p^{*\,2}_{\rm T,jets}$ (*left*) and of $x_{I\!P}$ (*right*), compared with the new and old [3] LO QCD fits.

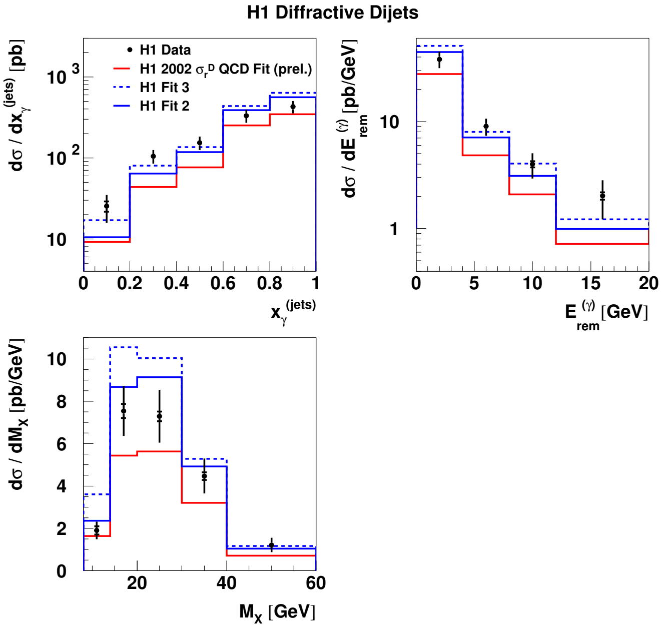

Figure A11: H1 measurements [11] of diffractive dijet cross sections differential in the fraction $x_\gamma^{\rm jets}$ of the virtual photon momentum transferred to the dijet system, the energy $E^{\gamma}_{\rm rem}$ in the photon hemisphere reconstructed outside the jets and $M_{\rm X}$, compared with the new and old [3] LO QCD fits.

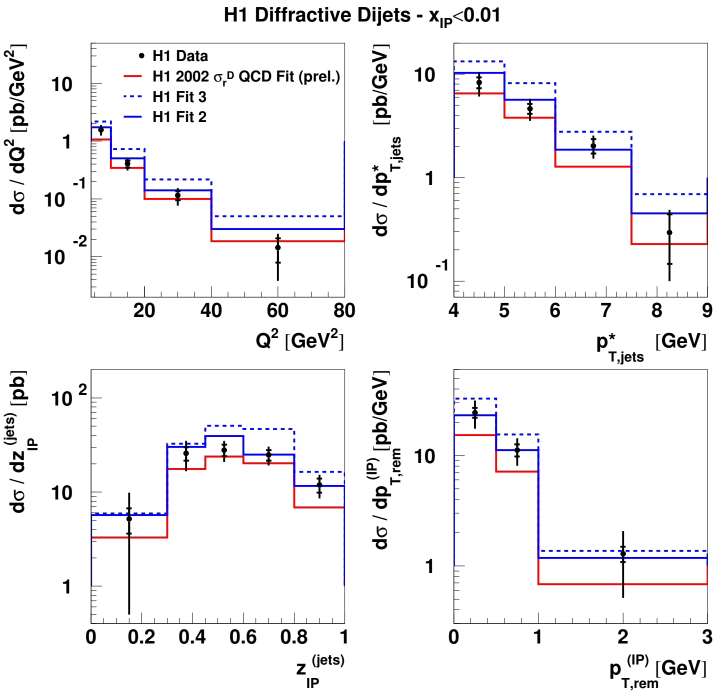

Figure A12: H1 measurements [11] of diffractive dijet cross sections in the restricted region $x_{I\!P} < 0.01$, compared with the new and old [3] LO QCD fits. The cross sections are shown differentially in Q^2, $p^*_{\mathrm{T,jets}}$, $z_{I\!P}$ and the transverse momentum $p^{I\!P}_{\mathrm{T,rem}}$ in the 'pomeron' hemisphere reconstructed outside the jets.

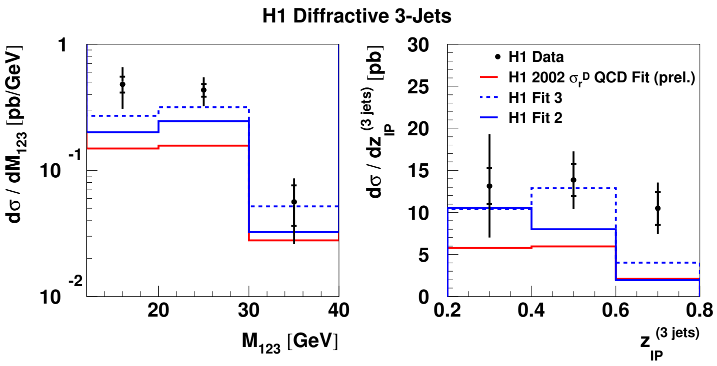

Figure A13: H1 measurements [11] of diffractive three-jet cross sections compared with the new and old [3] LO QCD fits with the same assumptions for the Monte Carlo modelling as in [11]. The cross sections are shown differentially in the three jet invariant mass M_{123} and in the fraction of the exchanged momentum transferred to the three-jet system $z_{I\!P}^{\mathrm{3jets}}$.

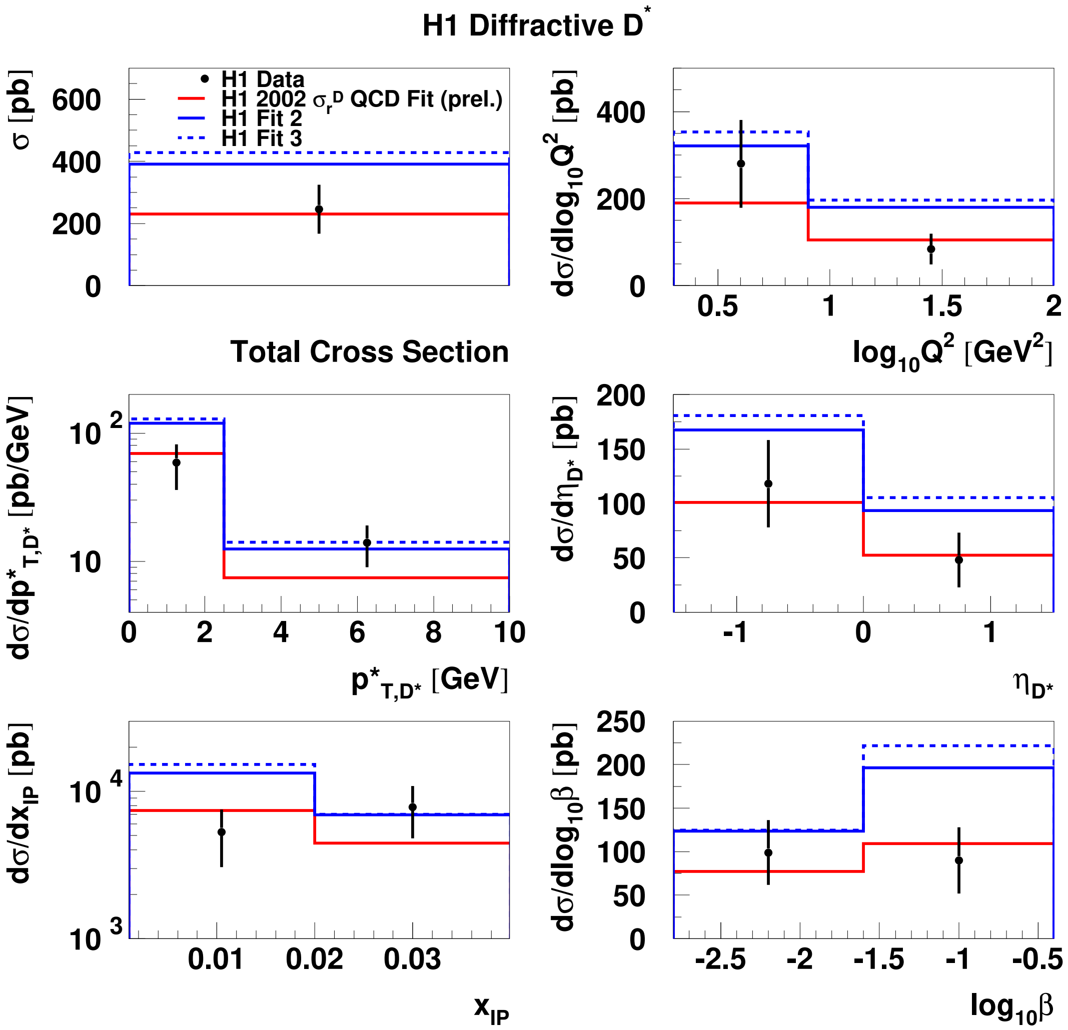

Figure A14: H1 measurements [12] of diffractive D^* production cross sections compared with the new and old [3] LO QCD fits with the same assumptions for the Monte Carlo modelling as in [12]. The cross section is shown integrated over the full measured phase space and differentially in $\log_{10} Q^2$, the transverse momentum of the D^* in the $\gamma^* p$ system, the pseudorapidity of the D^*, $x_{I\!P}$ and β.